



Neoproterozoic banded iron formation within a ~2620 Ma turbidite-dominated deep-water basin, Slave craton, NW Canada



Rasmus Haugaard^{a,1,*}, Luke Ootes^{b,c,2}, Kurt Konhauser^a

^a Department of Earth and Atmospheric Sciences, University of Alberta, Edmonton, AB, Canada

^b Northwest Territories Geological Survey, Box 1320, Yellowknife, NT X1A 2L9, Canada

^c Arctic Institute of North America, University of Calgary, 2500 University Drive NW, Calgary, AB, T2N 1N4, Canada

ARTICLE INFO

Article history:

Received 7 May 2016

Revised 27 November 2016

Accepted 23 January 2017

Available online 26 January 2017

Keywords:

Neoproterozoic

Slave craton

BIF

Seawater chemistry

Turbidites

Provenance

ABSTRACT

Banded iron formations (BIFs) are iron- and silica-rich chemical metasedimentary rocks that span much of the Archaean and early Palaeoproterozoic rock record. Given that BIFs precipitated from ambient seawater, they provide an important archive of Earth's ancient marine environments. Within the Slave craton occurs one of the largest and well-preserved Archaean turbidite basins in the world. Interstratified within the greywacke-mudstone turbidites is BIF that is commonly associated with ferruginous sediments and locally with a felsic tuff bed. Field investigations were conducted at four BIF locations from west to east across the Slave craton. These BIFs are composed of micro- and mesobands of quartz and magnetite, with various amounts of metamorphic grunerite, ferro-actinolite, ferro-hornblende as well as greenalite and stilpnomelane, the latter two are interpreted as retrograde metamorphic phases. As the BIF was deposited in a deep-water turbidite-dominated basin(s), the chemical component was occasionally diluted by clastic detritus, as illustrated by highly variable Al_2O_3 content, and Al_2O_3/TiO_2 and Cr/Ni that are similar to the clastic sediments. On a layer-by-layer basis, the iron content in the BIF ranges from as low as 4 wt.% and up to ~75 wt.% Fe_2O_3 , whereas the SiO_2 content ranges from 20 wt.% to as high as ~94 wt.%. This, together with a hyperbolic germanium/silicon distribution, suggests that continentally-sourced silica comprised the background precipitation, which was periodically interrupted by pulses of hydrothermally-sourced iron. High-temperature hydrothermal fluids contributed, with an average shale-normalized positive Eu anomaly of 1.92, which indicates input of reduced Eu^{2+} to the ambient seawater. The BIF shows characteristic aqueous fluid-derived rare earths + yttrium fractionation ($Pr/Yb < 1$) and positive La and Y anomalies. A negative Ce anomaly in parts of the BIF indicates the presence of an oxidizing agent able to fractionate Ce^{3+} to Ce^{4+} . The age and trace element signature of the felsic tuff is similar to arc-type volcanic rocks, potentially linking the BIF and turbidite basin (s) to the Defeat Suite plutons (ca. 2630–2620 Ma). The slow chemical rainout behind BIF deposition presumably took place on the basin plain adjacent to a steep submarine ramp where turbidite currents and slump-generated debris flows, sourced and triggered by the tectonically active arc-terrain, episodically delivered clastic sediment.

© 2017 Elsevier B.V. All rights reserved.

1. Introduction

Banded iron formations (BIF) are chemical sedimentary rocks that precipitated from marine waters throughout much of the Archaean and early Palaeoproterozoic (Bekker et al., 2013). The majority of Archaean BIFs consist of ~15–40 wt.% total iron and

~40–60 wt.% silica and typically contain alternating bands of chert and magnetite, or hematite with minor Fe-silicates, and typically range from small-scale laminated microbands (<1 cm thick) up to cm-scale mesobands (James, 1954; Trendall and Blockley, 2004; Klein, 2005; Haugaard et al., 2013; Haugaard et al., 2016b). Post-depositional processes, such as diagenesis and later metamorphism, modified the primary mineralogy of BIF and make any interpretation of the precursor sediment challenging. Minerals such as chert, hematite, magnetite, stilpnomelane, grunerite, actinolite, hornblende, calcite and dolomite-ankerite are all of diagenetic and of metamorphic origin (e.g., Bekker et al., 2013). Proposed primary minerals are amorphous silica, ferric

* Corresponding author.

E-mail address: rashaugaard@gmail.com (R. Haugaard).

¹ Current address: Vesterhavshytten, Rønnevej 18, 9690 Fjerritslev, Denmark.

² Current address: British Columbia Geological Survey, Box 9333, Stn Prov Govt, Victoria, BC V8W 9N3, Canada.

oxyhydroxide, siderite and, in some cases, greenalite (Klein, 2005). The amount of continentally derived detritus in BIF is sparse as they generally have low Al_2O_3 content (<1 wt.%) and other fluid-immobile elements (i.e., Ti, Zr, Nb, Th, and Hf). Compared to modern seawater, the shale-normalized rare earth element + yttrium (REY) pattern in most BIF show enrichment in the heavy-REE relative to the mid-REE and light-REE ($\text{HREE} > \text{MREE} > \text{LREE}$), consistent with the seawater origin of BIF (e.g., Byrne and Kim, 1990; Bolhar et al., 2004). The iron in BIF was likely sourced from submarine hydrothermal venting, where the ferrous iron (Fe^{2+}) could have been transported great distances under the strongly anoxic conditions of the oceans during the Archaean (Holland, 1973; Bekker et al., 2004; Bekker and Holland, 2012). An enrichment of reduced Eu^{2+} measured as a shale-normalized positive Eu anomaly in the BIF is evidence for this process (e.g., Bau and Möller, 1993). The dissolved iron was oxidized to Fe^{3+} in the photic zone by either abiological or biological oxidation and subsequently settled to the sea floor as a ferric oxyhydroxide, such as ferrihydrite, $\text{Fe}(\text{OH})_3$ (e.g., Bekker et al., 2010, 2014). Dissolved silica, on the other hand, was sourced from either continental weathering (Hamade et al., 2003) or hydrothermal alteration (Steinhofel et al., 2010; Bekker et al., 2013). The silica likely acted as a background sedimentation occasionally interrupted by pulses of iron rich water (e.g., Frei and Polat, 2007; Haugaard et al., 2013).

Since the deposition of BIF is restricted to the Precambrian, the puzzle of solving their origin and depositional environment are more likely to be understood by the interpretation of the interbedded volcanic and sedimentary rocks, both of which have modern analogues (e.g., Drever, 1974; Krapež et al., 2003; Pickard et al., 2004). Archaean turbidites show similar physical properties to their modern counterparts as they are dominated by the same structural units such as massive and normal graded greywacke-mudstone sequences. Where the sediment in Phanerozoic turbidites are dominated by epiclastic debris, the greywacke sediment in Archaean turbidites often contains a mixture of epiclastic and volcanoclastic debris that has been activated and shed from subaqueous slopes within tectonically active basins (Lowe, 1980; McLennan, 1984). The depositional relationship between the turbidites and BIF is enigmatic since the origin and rate of deposition for these two facies are highly different. Banded iron formation is believed to represent slow precipitation and settling of iron hydroxides and amorphous silica ($\text{Si}(\text{OH})_4$) from deep (>200 m) marine waters. For instance, well-studied depositional rates for Palaeoproterozoic Hamersley BIFs are on the average of 30 m (compacted)/1 million years (Pickard, 2002). Turbidites, on the other hand, represent dynamic and rapid sedimentation that can be measured within hours or days (e.g., Selley, 1988; Zane et al., 2012).

The turbidite-hosted BIF of the Slave craton, northwest Canada, are hosted within one of the largest and best-preserved Archaean sedimentary basins in the world (Padgham and Fyson, 1992). The timing of BIF deposition is now well-constrained to ca. 2620 Ma, from U-Pb zircon dating of an interbedded tuff bed (Haugaard et al., 2017). In this study, we present new petrologic and geochemical insights into the deposition of these Neoarchaean BIF. We interpret the seawater geochemical signature and relate this to the ambient palaeoenvironment and the role of the dominant sources controlling the seawater composition. As BIF is best understood in its depositional context, rather than as an isolated rock type, we also describe the interbedded turbidite deposits, as the origin and nature of these can be studied using modern analogues.

2. The BIF-bearing turbidites of the Slave craton

Approximately 70% of the Slave craton supracrustal rocks are composed of greywacke-mudstone turbidites (Padgham and Fyson, 1992). This Archaean turbidite basin(s) is one of the largest

and best preserved in the world, with deposition of up to 10 km of greywacke-mudstone cycles across an area of at least 32,000 km^2 (Ferguson et al., 2005; Bleeker and Hall, 2007; Ootes et al., 2009). The homogenous succession often lacks marker horizons, such as tuffaceous beds and lacks biostratigraphic units, making any subdivision of these turbidites difficult. Using detrital zircon deposition ages and new tuff ages, Ootes et al. (2009) and Haugaard et al. (2017) demonstrated that the turbidite basin in the central-western part of the craton could be subdivided into at least two temporally different “packages”. An older, turbidite succession that was deposited between ca. 2661–2650 Ma (Fig. 1; Duncan Lake Group; Bleeker and Villeneuve, 1995; Ferguson et al., 2005; Haugaard et al., 2017), and a younger succession that was deposited at ca. 2620 Ma (Slemon Group; Pehrsson and Villeneuve, 1999; Bennett et al., 2005; Ootes et al., 2009; Haugaard et al., 2017). Importantly these younger turbidites are distinctive as they locally contain interstratified BIF. Three depositional settings are proposed for the BIF-bearing turbidites from passive margin and foreland basin (Pehrsson, 2002), to accretionary wedge setting (Bennett et al., 2005), to a continental back-arc basin (Ootes et al., 2009). The latter model is supported by the fact that the timing of BIF and turbidite deposition coincides with the Defeat Suite plutons (ca. 2.62 Ga), interpreted as the root of a continental arc (Davis et al., 2003; Bleeker and Hall, 2007; Ootes et al., 2009).

2.1. Post-depositional history

The Slave craton experienced a complex history of magmatism and polyphase deformation and metamorphism during its evolution (Davis and Bleeker 1999; Bleeker and Hall, 2007; Helmstaedt 2009). The turbidite-BIF sequences were intruded by various generations of granitic plutons (Fig. 1B; e.g., van Breemen et al., 1992; Davis et al., 1994; Davis and Bleeker, 1999; Bennett et al., 2005; Ootes et al., 2005). Associated with the plutons are regional thermal metamorphic overprints that range from lower greenschist to granulite facies (e.g., Bennett et al., 2005). The latter has resulted in the development of various porphyroblasts in the turbidites, such as cordierite, garnet, and sillimanite. The BIF-bearing turbidites are also important host rocks for epigenetic lode-gold deposits (Padgham, 1992). Quartz and carbonate veining and a high-degree of hydrothermal alteration from sulfur-rich fluids resulted in the formation of gold-bearing iron sulfides (pyrrhotite, pyrite, and arsenopyrite) within the fold-hinges of tightly folded BIF horizons. These horizons provided favorable chemical and structural traps for gold-bearing hydrothermal fluids. The structural timing of this mineralization event is likely of syn- to late-metamorphic origin (ca. 2.59 Ga; Bleeker and Hall, 2007; Ootes et al., 2011).

3. Field observations

3.1. Slemon Lake

In the southwest Slave craton the Slemon Lake area is underlain by extensive greywacke-mudstone turbidites with locally interbedded BIF (Fig. 1; Jackson, 2001). The BIF-bearing outcrops are characterized by tightly folded and faulted sequences of inter-layered BIF and greywacke-mudstone sequences (Fig. 2A and B). The BIF layers are up to are 0.5 m thick and composed of finely laminated bands. Individual BIF units are commonly underlain and capped by 0.2 to 0.7 m thick greywacke beds (Fig. 2A).

The BIF has two scales of banding, microbanding (mm-scale) and mesobanding (cm-scale), the latter shows magnetite mesobands with internal mm-scale chert microbands (Fig. 2C). The best preserved outcrops have variable oxide (magnetite) content. Those

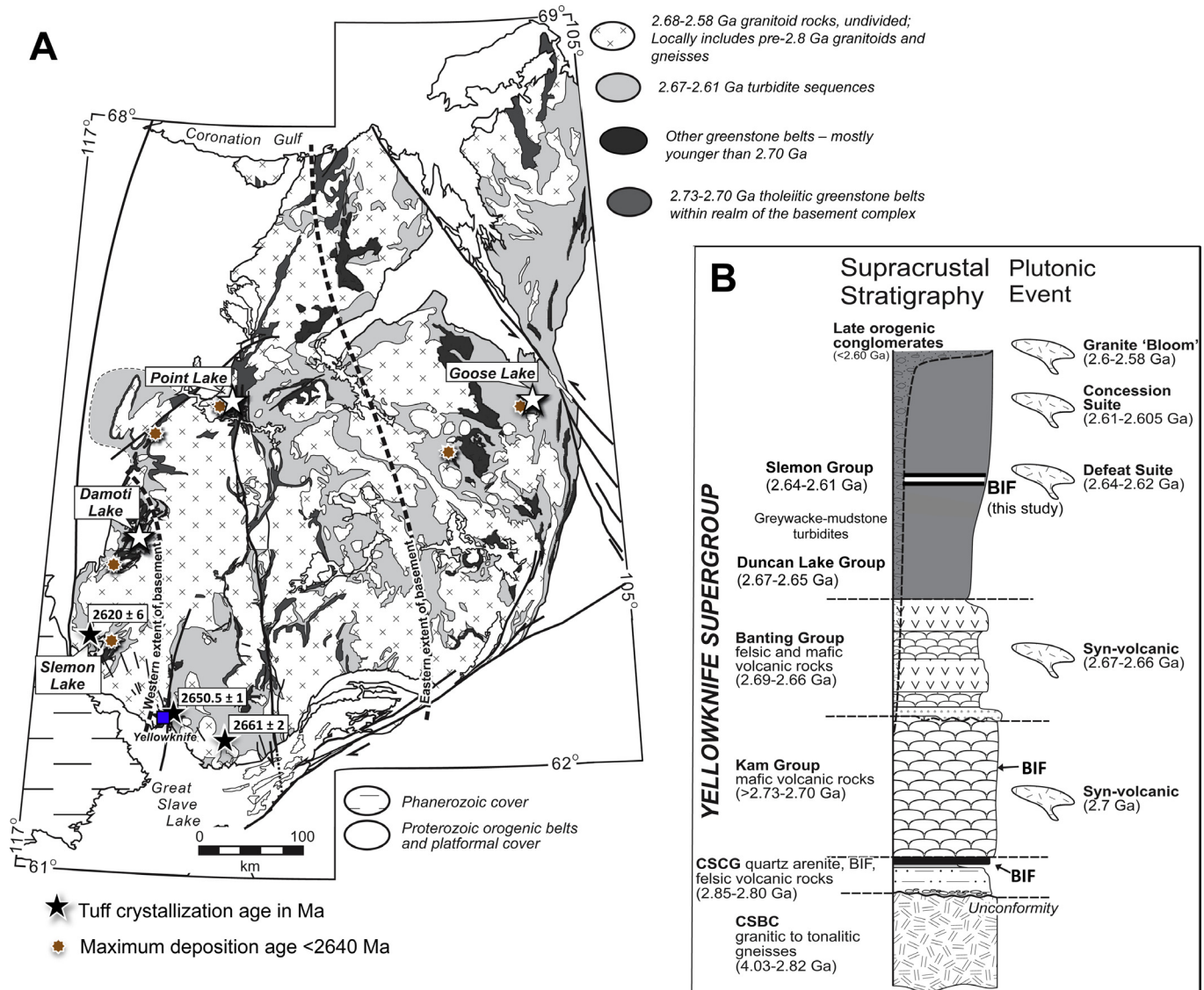


Fig. 1. (A) Geology of the Slave craton with the locations of this study. Note that the Slemon Lake location contains tuff beds with a crystallization age of ca. 2620 Ma (Slemon Group; Haugaard et al., 2017), which defines the age of the Slave craton Neoproterozoic BIF-turbidites. The crystallization age of tuff beds between ca. 2661 Ma to 2650 Ma defines the age of the older Duncan Lake Group turbidites (Bleeker and Villeneuve, 1995; Haugaard et al., 2017). (B) The supracrustal stratigraphy of the Slave craton with the major plutonic events illustrated. The Neoproterozoic BIF of this study is hosted within the Slemon Group greywacke-mudstone turbidites (Haugaard et al., 2017). CSBC = Central Slave Basement Complex; CSCG = Central Slave Cover Group. Map and stratigraphy modified after Bleeker (2002), Bleeker and Hall (2007), and Ootes et al. (2009).

with highest oxide content (Fig. 2A) show alternating bands of very fine-grained green chert and black magnetite (Fig. 2C), whereas the outcrops with less magnetite contain more silicates represented by bands of fine-to-medium grained green amphiboles and chert (Fig. 2D and E). The most weathered BIF outcrops show pervasive red hematite alteration as a result of secondary oxidation of magnetite (Fig. 2B). Above the BIF units, within the greywacke beds occur interbedded calc-silicate and semi-pelitic beds, up to 30 cm thick. The greywacke units commonly show a fining upward trend, which occasionally terminates with deposition of mudstone facies. In relation to this fining-upward trend, climbing ripples can be found in the fine-grained top part of the turbidites (Fig. 2F). The turbidite-BIF sequences at Slemon Lake are directly associated with synchronous volcanism, as indicated by a thin, (2–5 cm) yellow-weathered felsic-to-intermediate tuff bed (Fig. 2G). This bed has yielded a U-Pb zircon crystallization age of 2620 ± 6 Ma (Haugaard et al., 2017).

3.2. Point Lake

In the central Slave craton, the northeast side of Point Lake is underlain by extensive greywacke-mudstone turbidites with locally interbedded BIF (Fig. 1; Bostock 1980; Henderson, 1970). The BIF-bearing turbidities at Point Lake are characterized by alternating oxide BIF and greywacke with only minor mudstone beds (Fig. 3A and B). Each BIF unit ranges between 0.2 and 0.5 m in thickness (Fig. 3A and B). Where preserved, each BIF unit has a sharp and straight lower contact to the underlying greywacke, whereas the upper contact with the overlying greywacke is wavy and erosional in nature (Fig. 3B). A large proportion of the individual BIF units have well-developed ≤ 1 mm microbands of chert and magnetite, which illustrate the fine-scale nature of the BIF deposition (e.g., Fig. 3C). Individual greywacke units vary from small cm-scale beds to larger beds that are 1–1.5 m in thickness (Fig. 3A and B). The greywackes also range from being vertically

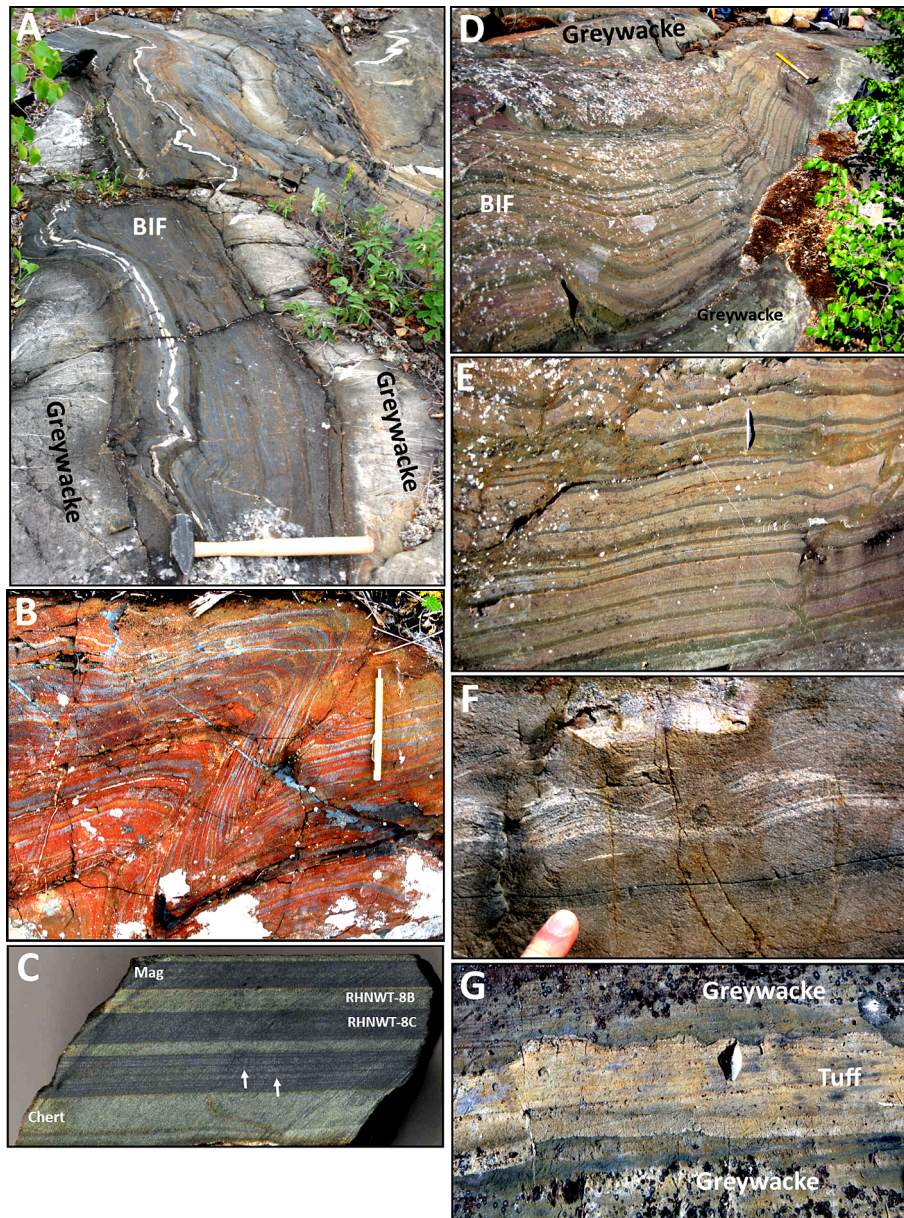


Fig. 2. Representative photographs of the Slemon Lake BIF occurrence. (A) Magnetite-rich BIF sandwiched by two sandy greywacke beds and offset along a fracture. (B) Tightly folded hematite-bearing BIF. (C) Close-up photograph of a fresh-cut sample showing alternating bands of magnetite (Mag) and silica (Chert). Note the microbands of chert within mesobands of magnetite (white arrows). The green tinted color in the silica bands is due to fine-grained silicates (mostly actinolite). The sample numbers represent the silica and iron bands separated for geochemical analysis (see Table 3). (D, E) Silicate-BIF with lesser amount of magnetite relative to (A). The green tinted color is due to the presence of actinolite. (F) Fine-scale climbing ripple lamination at the top of the greywacke unit. (G) Tuff bed within fine-grained greywacke/silty mudstone unit ~1 m above the BIF deposit in (D).

unstructured to having weakly defined fining-upward trend. During burial of the sediment package, the water-saturated fluidized greywacke sediment intruded the BIF and is now preserved as sedimentary dykes (Fig. 3D). Locally concordant and interstratified with the BIF horizons are thin (2–8 cm) mafic ferruginous beds containing coarse-grained black-to-dark green hornblende (Fig. 3E).

3.3. Damoti Lake

In the western Slave craton the Damoti Lake area is underlain by extensive greywacke-mudstone turbidites with locally interbedded BIF (Fig. 1) and the surrounding area is geologically complex with a multiphase deformational history. Within the cen-

tral part of the turbidite-BIF supracrustal belt the metamorphic facies ranges from lower greenschist to amphibolite grade (Pehrsson and Villeneuve, 1999); the BIF studied underwent greenschist facies metamorphism. The BIF shows large variations in both physical appearance and mineral composition. The best-preserved BIF (Fig. 4A) is within the central part of the belt, outside the zones of intense hydrothermal alteration. Parts of the BIF contain layers of silicate-facies BIF (grunerite-rich) that vary in thickness from a few centimeters to a few millimeters (Fig. 4B), while other parts are more homogenous and massive with a mixture of magnetite, chert, and radiating amphiboles.

Within the laminated to bedded BIF, early diagenetic chert nodules show evidence of differential compaction as indicated by the curved microbands around them (Fig. 4C). Graded greywacke and

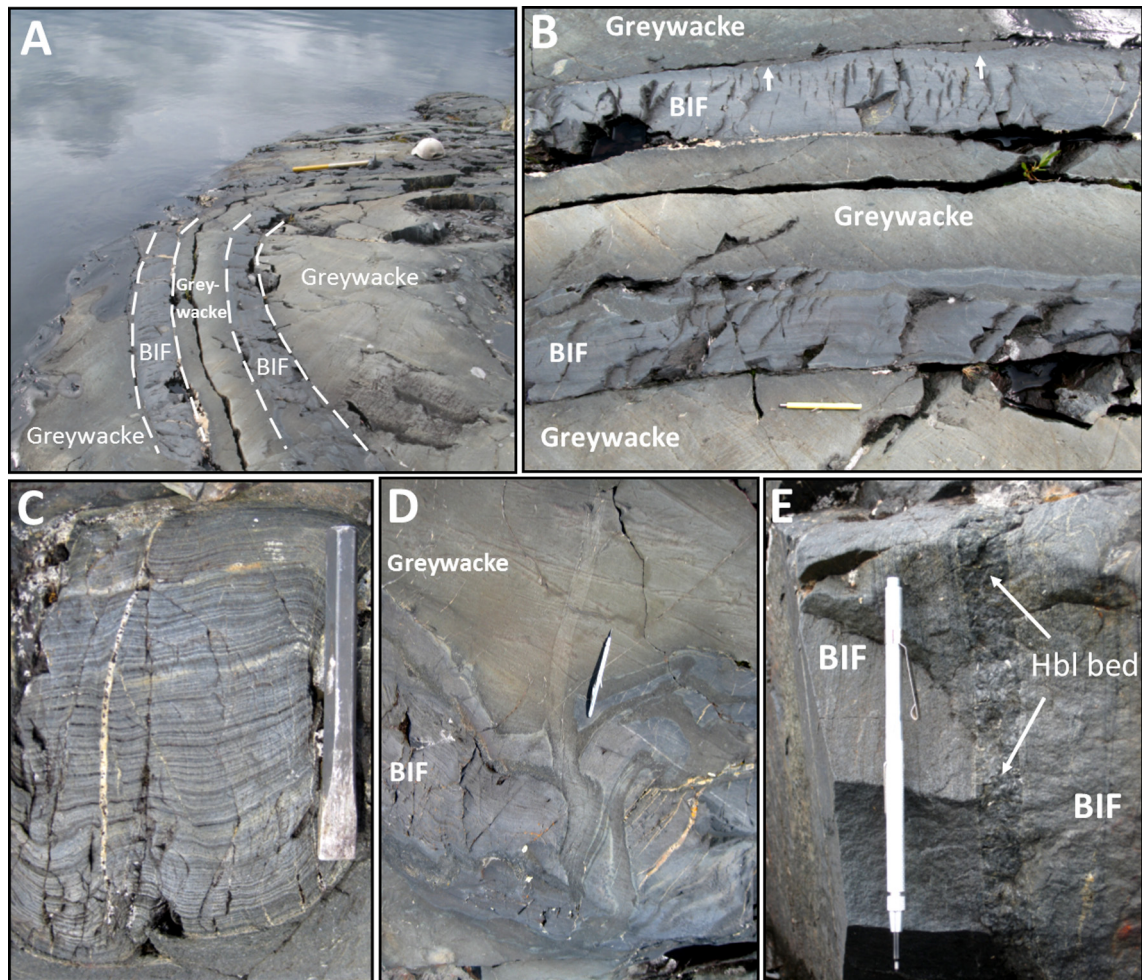


Fig. 3. Representative photographs of the Point Lake BIF. (A, B) BIF interbedded with sandy greywacke. The BIF within the greywackes has a flat and sharp lower contact and, where preserved, a wavy and erosional upper contact (white arrows in B). (C) Fine-scale microbands of the oxide-BIF. (D) Sedimentary dyke generated when the sediment was still wet during burial and compaction. (E) Ferruginous bed consisting of dark, coarse-grained hornblende parallel to bedding in the BIF.

mudstone beds occur stratigraphically below and above the BIF units. Similar to Point Lake, the BIF is associated with dark-greenish and dark- to silver-grey ferruginous beds ranging in composition from almost pure coarse-grained amphibole to more fine-grained beds containing amphibole with randomly distributed biotite porphyroblasts (1–2 mm in size; Fig. 4D). Some layers contain minor graphite, which gives the rock a metallic luster (Fig. 4D). Stratigraphically, these ferruginous beds occur at the base of the greywacke-mudstone turbidites immediately above the BIF unit (Waychison, 2011). The ferruginous beds contain both detrital magnetite grains and rip-up clasts from the BIF itself (Waychison, 2011). The ferruginous sediment locally shows variations in grain size over an outcrop scale of only 20–50 cm where the hornblende and grunerite ranges from very coarse-grained (~1–1.5 cm) to more fine-grained (1–2 mm; Fig. 4D).

3.4. Goose Lake

In the eastern Slave craton the Goose Lake area is underlain by extensive greywacke-mudstone turbidites with locally interbedded BIF (Fig. 1; Frith, 1987). Where exposed, the BIF at Goose Lake is characterized by centimeter-scale mesobands of chert, alternating with magnetite with intergrown radiating amphiboles (Fig. 4E). In outcrop, the Goose Lake BIF is visually similar to the BIF at Damoti Lake (Fig. 4A). Drill core-samples obtained from the

least-altered zones show individual BIF units (chert + magnetite + amphibole bands) that vary in thickness from 10 to 50 cm. The magnetite bands range from millimeter scale up to 2 cm in thickness (Fig. 4F). The thickness of the alternating chert bands range from millimeters up to 5 cm in thickness (Fig. 4F). Typically, at the magnetite-chert interface, dark-to-pale green to colorless radiating amphiboles (actinolite + grunerite) occur (Fig. 4F). Brown stibnomelane is locally found in association with the pale-green amphiboles (Fig. 4F).

The associated greywackes contain fine- to medium-grained, quartz-rich sand and have stratigraphic thicknesses ranging from 0.25 to 3 m. Parts of the greywackes preserve a weakly graded (fining upward) trend, while others are vertically massive with uniform grain size distribution (Fig. 5). The greywackes often transition into 10 to 20 cm thick clay- and silt-rich mudstone beds that form sharply bounded couplets (Fig. 5). However, exceptions do occur where the turbidites lack the mudstone facies and only consist of fine-grained greywacke deposits interbedded with BIF (Fig. 5). Locally the mudstone is weakly magnetic, and contains graphite and visible chlorite.

4. Samples and analytical techniques

BIF samples suitable for separation of individual chert- and magnetite-bands were obtained at Slemon Lake and from the

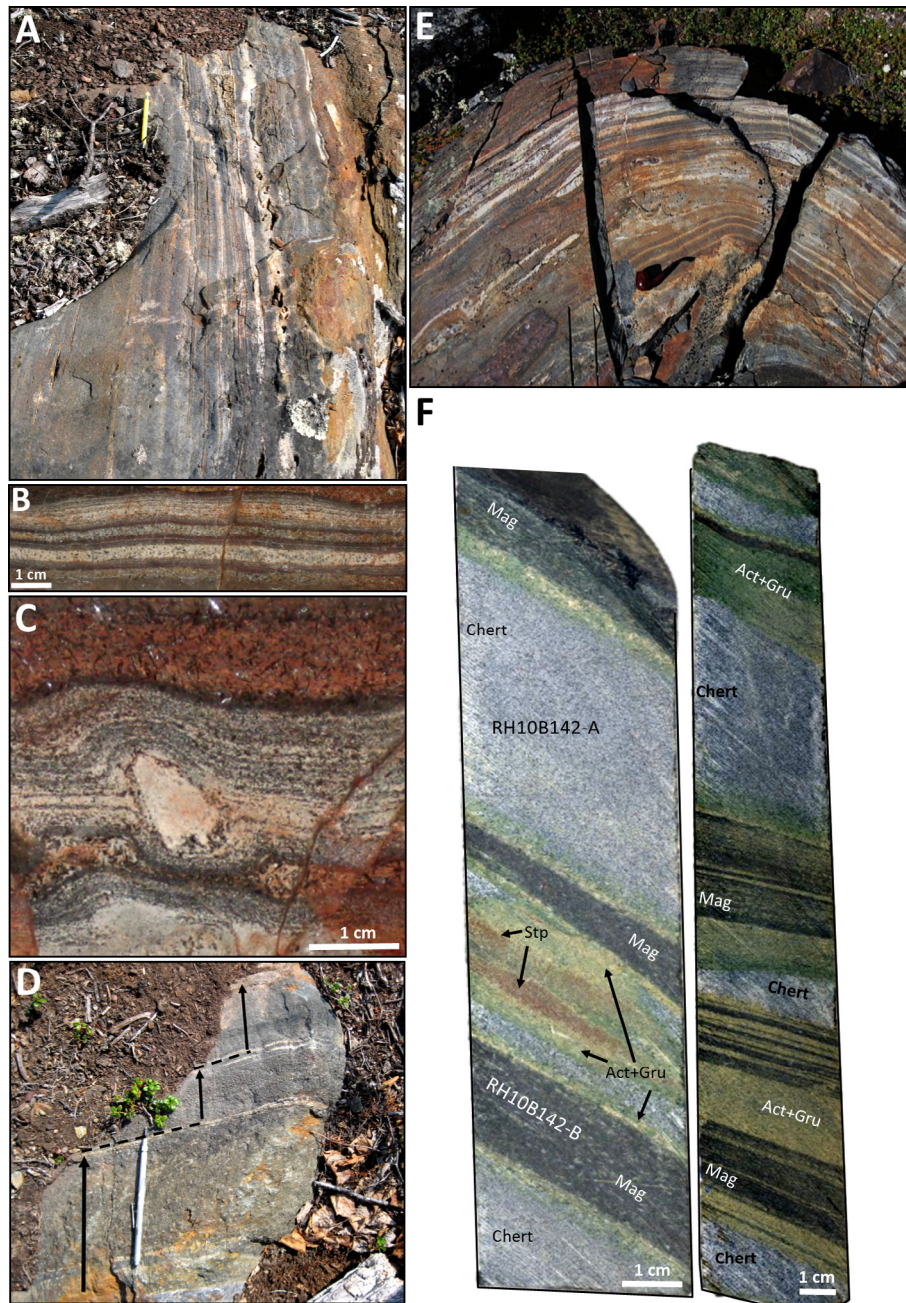


Fig. 4. Representative photographs of the Damoti and Goose Lake BIF occurrences. (A) A BIF outcrop at Damoti Lake showing alternating chert and magnetite mesobands. (B, C) Close-up photographs showing magnetite microbands within chert mesobands. The mesobands contain radiating grunerite crystals (upper part of C). In (C), differential compaction during late-diagenesis resulted in bedding enveloping chert nodule. (D) Hornblende-rich ferruginous sediment showing three beds each with significant different crystal size from coarse grained up to fine-grained. The upper, finer-grained grey, weathered beds contain biotite porphyroblasts, plagioclase, and graphite. (E) The Goose Lake BIF showing a similar style of mesobands as at Damoti Lake. (F) Pristine drill-core samples from Goose Lake with amphibole growth at the magnetite chert interface. Note the thicker chert bands relative to the magnetite bands. The sample numbers represent the silica and iron bands separated for geochemical analysis (see Table 3). Ch = chert, mag = magnetite, gru = grunerite, act = actinolite, stp = stilpnomelane.

Goose Lake drill cores. These are labelled with the letter A (Si) and B (Fe) in Table 3. Due to the microbanded nature of the Point Lake BIF and the difficulties in separating bands from Damoti Lake, only the bulk BIF geochemical results from these two locations are presented. The separation of individual bands was completed with a diamond saw blade (10 cm \varnothing). The crushed BIF and associated rock samples were analyzed using the Code 4 Litho fusion-XRF and trace elements were analyzed by fusion-ICP-MS at the Activation Laboratories, Ancaster, ON. Repetitive analysis of internal standards yielded accuracy better than $\pm 10\%$, and often better than $\pm 5\%$. Precision on the duplicate samples is within $\pm 5\%$.

Backscatter electron images, elemental distribution maps, EDS (energy dispersive spectrometry) and WDS (wavelength dispersive spectrometry) were obtained with a JEOL Microprobe 8900 at the University of Alberta, Edmonton, AB. The machine parameters were set to a current of 30 nA and the probe beam diameter was 2 μm . Counting time was 30 s on peak, and 15 s on background. Amphibole calculations were completed using Loco (2014). For greenalite, all Fe is assumed to occur as FeO, which is in agreement with other studies (e.g., Gole, 1980a,b; Klein and Gole, 1981). Stilpnomelane, on the other hand, is more complex and can accommodate both oxidation states of Fe (see Eggleton and Chappell, 1978

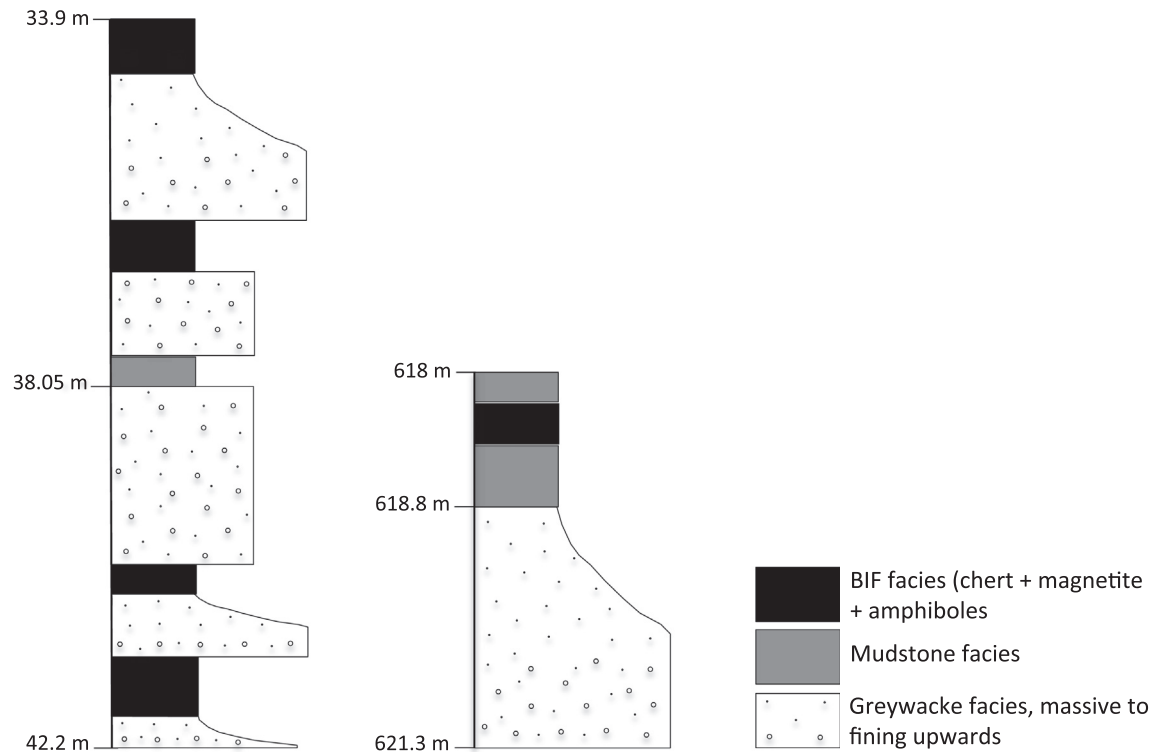


Fig. 5. Examples of the lithostratigraphy of two core sections from Goose Lake that illustrate the relationship between the BIF and the greywacke-mudstone turbidites. Note that BIF do not exist between all greywacke-mudstone sequences and not all greywacke units terminate with mudstone facies either. This is presumably due to either lack of preservation, time between cycles or changes in the distance to the sediment source. See text for further details.

Table 1
Amphiboles - mineral data from the BIF and the interbedded ferruginous sediment.

Analysis (wt%)	BIF			Ferro-actinolite			BIF/Ferruginous sediment		
	Grunerite			Ferro-actinolite			Ferro-hornblende		
	Min	Max	Ave	Min	Max	Ave	Min	Max	Ave
SiO ₂	49.49	50.08	49.87	47.92	50.92	49.54	40.09	46.01	42.07
TiO ₂	0.00	0.01	0.00	0.00	0.06	0.02	0.01	0.33	0.14
Al ₂ O ₃	0.10	0.52	0.25	1.28	3.96	2.39	5.61	16.45	12.71
Cr ₂ O ₃	0.00	0.02	0.01	0.00	0.02	0.01	0.00	0.10	0.02
MnO	0.16	0.23	0.20	0.05	0.08	0.07	0.04	0.19	0.12
FeO	43.32	45.27	44.14	27.36	31.45	28.87	20.08	28.91	23.31
Fe ₂ O ₃	0.00	0.30	0.04	0.93	3.52	2.11	1.78	5.21	3.58
MgO	3.10	4.18	3.52	3.67	5.16	4.45	1.65	5.87	3.81
CaO	0.49	1.30	0.76	10.60	11.51	11.26	11.10	11.56	11.33
SrO	0.00	0.03	0.00	0.00	0.08	0.05	0.00	0.05	0.01
Na ₂ O	0.00	0.09	0.05	0.20	0.50	0.32	0.71	1.68	1.33
K ₂ O	0.00	0.04	0.01	0.05	0.21	0.12	0.32	0.77	0.44
H ₂ O ⁺	1.85	1.86	1.85	1.91	1.93	1.92	1.88	1.97	1.94
Cl	0.0000	0.0170	0.0035	0.0000	0.0120	0.0052	0.0000	0.0280	0.0037
Total	99.94	101.15	100.72	100.94	101.39	101.15	99.86	101.58	100.81
<i>Formula assignments – based on 24 (OH, F, Cl, O)</i>									
Si	7.93	8.04	8.00	7.41	7.81	7.64	6.17	7.19	6.46
Al	0.01	0.07	0.04	0.19	0.59	0.36	0.81	1.84	1.54
Ti	0.00	0.00	0.00	0.00	0.01	0.00	0.00	0.04	0.02
Al	0.02	0.05	0.03	0.04	0.13	0.08	0.22	1.14	0.75
Cr	0.00	0.00	0.00	0.00	0.00	0.00	0.00	0.01	0.00
Fe ³⁺	0.01	0.03	0.02	0.11	0.41	0.24	0.20	0.62	0.42
Fe ²⁺	3.96	4.24	4.12	3.48	3.89	3.65	2.49	3.72	2.95
Mg	0.74	0.99	0.84	0.85	1.18	1.02	0.39	1.32	0.87
Mn ²⁺	0.02	0.03	0.03	0.01	0.01	0.01	0.01	0.03	0.02
Fe ²⁺	1.74	1.85	1.80	0.04	0.19	0.08	0.03	0.10	0.05
Ca	0.08	0.22	0.13	1.76	1.89	1.86	1.81	1.92	1.86
Sr	0.00	0.00	0.00	0.00	0.01	0.00	0.00	0.01	0.00
Na	0.00	0.03	0.01	0.03	0.07	0.05	0.04	0.10	0.07
Na	0.00	0.01	0.01	0.03	0.08	0.05	0.14	0.43	0.33
K	0.00	0.01	0.00	0.01	0.04	0.02	0.06	0.15	0.09
OH	2.00	2.00	2.00	2.00	2.00	2.00	1.99	2.00	2.00
Cl	0.0010	0.0050	0.0026	0.0010	0.0030	0.0025	0.0010	0.0070	0.0019

Table 2
Greenalite and stilpnomelane – mineral data from the Goose Lake BIF.

	Greenalite [*]			Stilpnomelane [#]		
	Min	Max	Ave	Min	Max	Ave
SiO ₂	34.55	35.58	35.23	41.35	45.04	44.08
TiO ₂	0.00	0.02	0.01	0.00	0.02	0.00
Al ₂ O ₃	0.14	1.97	0.71	4.62	6.49	6.05
FeO	49.57	52.85	51.93	31.85	35.80	32.91
Fe ₂ O ₃	–	–	–	3.93	4.42	4.06
Cr ₂ O ₃	0.00	0.04	0.01	0.00	0.04	0.01
MnO	0.11	0.20	0.16	0.04	0.08	0.06
MgO	0.89	1.23	1.07	1.59	2.05	1.74
CaO	0.01	0.12	0.05	0.04	0.37	0.11
Na ₂ O	0.01	0.07	0.03	0.36	1.61	0.94
K ₂ O	0.00	0.18	0.03	2.01	4.10	2.79
Cl	0.48	1.05	0.77	0.03	0.17	0.08
H ₂ O calc	9.72	11.24	10.04	7.28	8.54	7.77
O = F,Cl	–0.24	–0.11	–0.17	–0.04	–0.01	–0.02
Total	97.83	100.95	99.88	98.52	101.87	100.18
	Formula assignments based on 14 oxygen equivalent (10 oxygen and 8 OH,F,Cl)			Formula assignments based on 15 octahedral and tetrahedral cations and 27 (O,OH,F,Cl)		
	Min	Max	Ave	Min	Max	Ave
Si	4.11	4.30	4.21	7.52	7.94	7.83
Al	0.00	0.00	0.00	0.99	1.24	1.11
Al	0.02	0.28	0.10	0.00	0.28	0.16
Ti	0.00	0.00	0.00	0.00	0.00	0.00
Fe ²⁺	5.09	5.29	5.20	4.70	5.44	4.89
Fe ³⁺	–	–	–	0.52	0.60	0.54
Mn	0.01	0.02	0.02	0.01	0.01	0.01
Mg	0.16	0.22	0.19	0.43	0.54	0.46
Ca	0.00	0.02	0.01	0.01	0.07	0.02
Na	0.00	0.02	0.01	0.12	0.55	0.32
K	0.00	0.03	0.00	0.46	0.95	0.63
O	10.00	10.00	10.00	19.85	21.35	20.92
OH	7.78	7.90	7.84	5.63	7.12	6.05
Cl	0.10	0.22	0.16	0.01	0.05	0.03
H ₂ O	–	–	–	1.50	1.64	1.58

^{*} Final weight percent values with H₂O calculated from OH content. Total Fe as Fe²⁺ only.

[#] Final weight percent values with H₂O calculated from OH content. Oxidation state of Fe assumed to be Fe³⁺/(Fe²⁺ + Fe³⁺) = 0.1.

and references therein). As such, stilpnomelane often contains various amount of Fe³⁺, either originating from the primary mineral growth or introduced later during weathering and alteration. On the basis of the reported literature (e.g., Klein, 1974 and references therein), we assume an average Fe³⁺/ΣFe of 0.1 as the best approximation.

5. Petrographic and mineralogical results

5.1. Banded iron formation

The size of the quartz- and magnetite-grains is typically <0.1 mm, with a small fraction of the magnetite occurring as larger ≤0.5 mm grains. The microcrystalline quartz creates a tight mosaic and the magnetite bands are compact with sharply defined boundaries with the silica-rich bands. Most of the magnetite bands are opaque, but minor parts of the bands have interlayered microcrystalline quartz microbands.

Together with the typical chert and iron oxide component, the BIF samples all contain variable amount of silicates. Electron microprobe analysis reveals that the majority of the silicates are in the form of grunerite and ferro-actinolite, with minor greenalite and stilpnomelane (Tables 1 and 2; Fig. 6). At Slemon Lake, very fine-grained actinolite and lesser chlorite are interspersed within many of the chert bands. This gives the bands a greenish tint in outcrop and hand sample (Fig. 2C). The actinolite and chlorite constitute up ~15–30% of the modal mineralogy in the chert bands and well-developed amphiboles are found in the Damoti and Goose Lake BIF, where up to 1 cm radiating grunerite crystals grew

perpendicular to the original bedding planes of the BIF. In detail, at Goose Lake, the amphibole bands at the interface between chert and magnetite bands represent a metamorphic product between the two latter minerals (Fig. 7A, B and C). The grunerite typically grows on, and outwards, from the magnetite bands, whereas actinolite starts growing further into the chert bands where magnetite becomes less abundant. The actinolite ranges from stubby to radiating and to perfect diamond-shaped crystals (Fig. 7D). In addition to the grunerite and actinolite, a network of fine-grained subhedral ferro-hornblende exists within magnetite microbands at both Point Lake and Goose Lake. At the latter location, both greenalite and stilpnomelane are developed as retrograde phases in association with grunerite and actinolite (Fig. 7E and F). The greenalite forms patches with diffuse grain boundaries filling out small spaces between well-crystallized amphiboles (Fig. 7E), whereas stilpnomelane typically occurs as cross-cutting sheaves and needles developed on the edge of larger grains of actinolite (Fig. 7E and F).

5.2. Tuff and ferruginous beds

5.2.1. Tuff bed (Slemon Lake)

The 5 cm thick ash tuff bed at Slemon Lake (2620 ± 6 Ma; Haugaard et al., 2017) contains randomly distributed fine-grained (≤100 μm) quartz fragments set in a very fine-grained (≤20 μm) quartz, biotite, chlorite, and feldspar groundmass (Fig. 7G and H). The minerals are distributed homogeneously with no particular grading, but the biotite and chlorite preserve a weak crenulation foliation.

Table 3
Selected major and trace elements in the BIF

Sample	Slemon Lake			Damoti Lake		Point Lake			Goose Lake							
	8A (bulk)	8B (Si)	8C (Fe)	22A (bulk)	22C (bulk)	29B (bulk)	29C-1 (bulk)	29D-1 (bulk)	12140-A (Si)	12140-B (Fe)	10142-A (Si)	10142-B (Fe)	10B142-A (Si)	10B142-B (Fe)	24164 (bulk)	
<i>Element (wt.%) D.L.</i>																
SiO ₂	0.01	45.13	68.65	32.97	66.67	53.64	53.08	49.15	46.78	92.86	25.77	80.02	20.3	93.68	22.68	45.38
Al ₂ O ₃	0.01	2.96	5.39	2.21	1.39	1.58	1.11	1.49	1.07	0.08	2.15	0.41	1.62	0.08	0.98	1.19
Fe ₂ O ₃ (t)	0.01	48.36	15.78	63.36	29.78	43.72	41.58	47.93	51.81	4.12	64.31	17.15	74.62	4.76	72.75	50.99
TiO ₂	0.001	0.124	0.191	0.098	0.06	0.081	0.043	0.042	0.045	<D.L.	0.096	0.008	0.072	<D.L.	0.052	0.049
MgO	0.01	1.51	2.83	1.03	1.16	1.28	0.4	0.78	0.56	0.22	1.92	1.25	1.33	0.35	0.88	2.07
CaO	0.01	0.9	1.86	0.24	0.16	0.28	3.02	1.73	1.09	1.36	5.68	1.08	1.93	0.3	2.49	2.4
Na ₂ O	0.01	< D.L.	< D.L.	< D.L.	0.03	0.08	0.12	0.13	0.07	0.01	0.21	0.05	0.15	0.01	0.1	0.11
K ₂ O	0.01	0.98	0.81	1.89	0.81	0.55	0.04	0.08	0.05	0.01	0.22	0.04	0.18	0.01	0.07	0.06
MnO	0.001	0.036	0.055	0.027	0.019	0.025	0.047	0.043	0.042	0.015	0.088	0.025	0.04	0.011	0.061	0.041
P ₂ O ₅	0.01	0.4	0.14	0.2	0.02	0.05	0.15	0.15	0.08	0.12	0.17	< D.L.	0.16	< D.L.	0.57	0.15
LOI		0.37	3.31	-0.8	-0.37	-0.8	0.56	-1.08	-1.56	1.1	-1.69	-0.46	-1.21	0.01	-1.75	-2
Total		100.8	100.1	100.1	99.47	100.5	100.1	100.4	100	99.9	98.91	99.55	99.2	99.21	98.91	100.4
Zr (ppm)	1	17	25	13	6	8	6	7	7	1	13	1	10	2	7	7
Nb	0.2	2.2	1.7	1.5	1.8	1.6	2	1.5	1.2	2.4	1.3	2.8	1	1.7	0.8	1.1
Th	0.05	1.25	2.1	0.95	0.51	0.57	0.46	0.42	0.54	0.06	1.09	0.06	0.77	0.1	0.48	0.52
Hf	0.1	0.5	0.7	0.3	0.2	0.2	0.2	0.2	0.2	< 0.1	0.4	< 0.1	0.2	< 0.1	0.2	0.2
Rb	1	47	88	40	64	61	1	3	< D.L.	< D.L.	6	< D.L.	8	< D.L.	2	2
Sc	0.01	3.94	5.62	3	2.31	2.47	1.48	1.62	1.61	0.42	3.53	0.24	2.69	0.84	1.8	2.13
Cr	0.5	31.5	45	27.6	15.8	17.3	19.6	19.7	25.5	< 0.5	24.9	< 0.5	19.1	< 0.5	16.1	19.5
Ni	1	25	30	19	11	11	11	14	10	2	17	3	12	4	10	11
V	5	33	19	39	18	22	15	20	13	< D.L.	30	< D.L.	22	5	17	15
Ta	0.01	1.77	0.15	0.09	4.27	4.07	4.89	3.21	2.43	7.48	1.11	8.1	0.92	5.25	0.81	1.73
Ge	0.5	5	2.8	5.7	3.7	4.3	2.1	2.5	2.5	1.4	7.4	1	6.8	2.2	8.8	7
U	0.01	0.46	0.57	0.42	0.13	0.22	0.13	0.18	0.16	0.03	0.25	0.02	0.21	0.05	0.18	0.12
Mo	2	< D.L.	< D.L.	< D.L.	< D.L.	< D.L.	< D.L.	< D.L.	< D.L.	< D.L.	< D.L.	< D.L.	< D.L.	< D.L.	< D.L.	< D.L.
S (%)	0.001	0.067	0.106	0.014	0.007	0.005	0.003	0.007	0.032	0.017	0.01	0.008	1.03	0.171	0.651	0.091
La	0.05	8.42	10.1	10	3.13	1.69	3.35	4.73	3.03	1.93	5.38	0.37	5.74	0.97	5.76	2.79
Ce	0.05	13.9	16.9	14.4	5.02	3.13	5.01	8.19	4.68	2.91	9.96	0.52	11.1	1.48	10.8	5.45
Pr	0.01	1.46	1.77	1.44	0.49	0.41	0.54	0.87	0.41	0.31	1.19	0.06	1.33	0.17	1.25	0.67
Nd	0.05	5.59	6.78	5.23	1.63	1.61	2.06	3.11	1.26	1.48	4.8	0.26	5.32	0.65	5.2	2.62
Sm	0.01	1.01	1.25	0.87	0.35	0.32	0.38	0.49	0.22	0.33	1.04	0.03	1.23	0.15	1.16	0.67
Eu	0.005	0.328	0.518	0.258	0.19	0.12	0.29	0.202	0.112	0.229	0.534	0.025	0.376	0.064	0.415	0.279
Gd	0.01	0.99	1.21	0.71	0.46	0.33	0.43	0.62	0.25	0.28	1.16	0.04	1.56	0.17	1.61	0.79
Tb	0.01	0.18	0.22	0.12	0.07	0.06	0.07	0.1	0.05	0.04	0.2	< 0.01	0.26	0.04	0.28	0.11
Dy	0.01	1.19	1.47	0.79	0.51	0.36	0.41	0.61	0.34	0.27	1.24	0.04	1.72	0.27	1.87	0.81
Y	2	10	11	5	4	3	3	4	3	4	9	4	12	<D.L.	15	7
Ho	0.01	0.28	0.33	0.18	0.11	0.09	0.09	0.14	0.08	0.06	0.27	< D.L.	0.4	0.06	0.42	0.19
Er	0.01	0.91	1.06	0.58	0.32	0.29	0.27	0.45	0.25	0.2	0.86	0.03	1.25	0.2	1.32	0.63
Tm	0.005	0.141	0.183	0.093	0.049	0.052	0.042	0.072	0.046	0.03	0.139	0.006	0.203	0.037	0.191	0.102
Yb	0.01	0.97	1.34	0.63	0.34	0.38	0.26	0.52	0.29	0.18	0.97	< D.L.	1.32	0.25	1.18	0.62
Lu	0.002	0.163	0.227	0.104	0.059	0.058	0.036	0.08	0.043	0.027	0.158	0.007	0.208	0.035	0.187	0.102
ΣREE		35.5	43.4	35.4	12.7	8.9	13.2	20.2	11.1	8.3	27.9	1.4	32.0	4.5	31.6	15.8
(Pr/Yb) _{NASC}		0.59	0.52	0.90	0.57	0.42	0.81	0.66	0.55	0.68	0.48	-	0.40	0.27	0.42	0.42
(La/		1.22	1.21	1.36	1.12	0.91	1.31	1.04	1.19	2.15	1.04	1.65	0.98	0.91	1.20	1.13
La*) _{NASC}																
(Eu/		1.40	1.80	1.40	2.24	1.59	3.26	1.69	2.00	3.40	2.15	-	1.24	1.85	1.56	1.37
Eu*) _{NASC}																
Y/Ho		35.7	33.3	27.8	36.4	33.3	33.3	28.6	37.5	66.7	33.3	-	30.0	-	35.7	36.8

Dark grey = Fe bands, light grey = bulk BIF, white = silica bands; D.L. = detection limit.

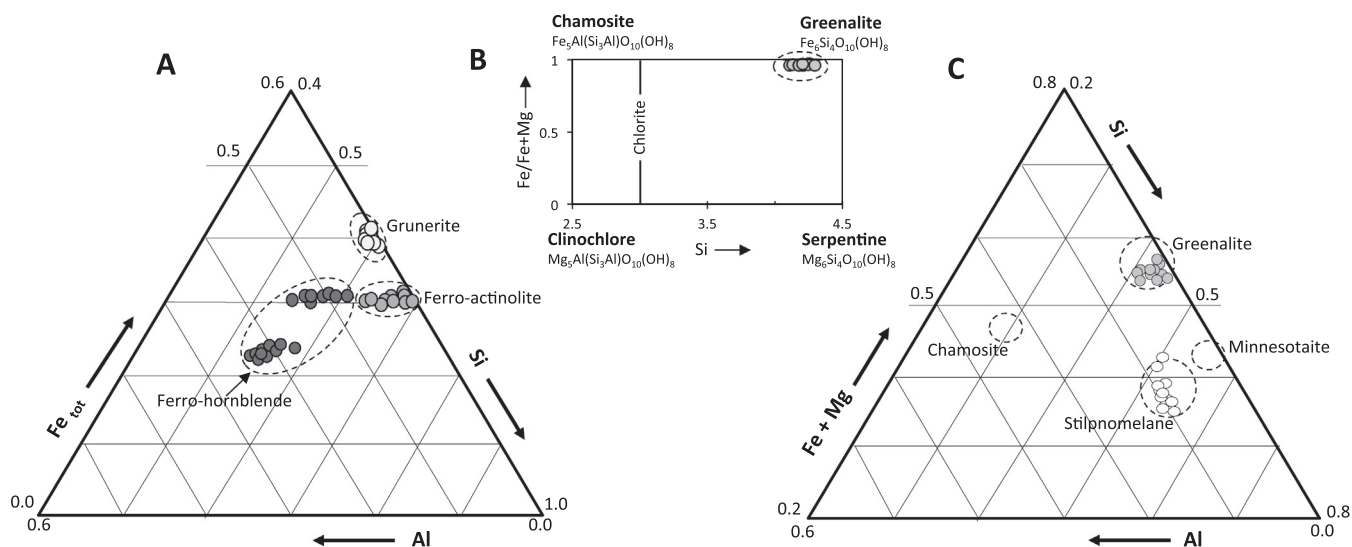


Fig. 6. Compositional diagrams illustrating the mineral composition of the BIF. (A) Ternary diagram showing the two main amphiboles (grunerite and ferro-actinolite) in the BIF. Ferro-hornblende, which has significantly more alumina, is mostly restricted to the associated clastic ferruginous beds. (B) The compositional relationship between the greenalite from Goose Lake BIF and related phases of chamosite, clinocllore, and serpentine. (C) Ternary diagram showing the retrograde greenalite and stilpnomelane from the Goose Lake BIF. Source of diagrams from Gole (1980) and McSwiggen and Morey (2008).

5.2.2. Ferruginous beds

In contrast to the monotonous greywacke-mudstone turbidites, ferruginous beds vary significantly in their texture and mineralogy, but collectively they all contain iron-rich phases such as chlorite, Fe-amphiboles, and biotite, with lesser amount of quartz. At Point Lake, these beds contain coarse-grained, euhedral ferro-hornblende (Figs. 6C, 8A; Table 1). The hornblende, which makes up approximately 25–35% of the rock by volume, is found randomly interspersed with medium-grained quartz rock fragments and alkali-feldspar all set in a very fine-grained biotite groundmass (Fig. 8A). Both hornblende and biotite have multiple inclusions of zircons and/or monazite. The stubby-to-prismatic hornblende is clearly of metamorphic origin as they engulf fragmented quartz crystals (Fig. 8A) and likely grew after the main deformation as they are randomly distributed with no fabric development. The ferruginous beds at Damoti Lake only contains small amount of quartz. Instead they contain randomly distributed biotite porphyroblasts (up to 2–3 mm in size) and fine-grained (≤ 1 mm) angular to subangular plagioclase set in a chlorite groundmass (Fig. 8B and C). Grunerite crystals up to 3 mm in size, with ferro-hornblende overgrowths, are disseminated throughout (Fig. 8D).

The overall plagioclase composition in the ferruginous beds is \sim An₁₃ (=oligoclase), although some grains are zoned and have a Ca-rich core and Na-rich rim. The plagioclase grains are locally accompanied by another feldspar, namely slawsonite, a Sr-bearing plagioclase. These slawsonite grains form aggregates and mosaic networks with poorly developed crystal shapes (Fig. 8C). Other Sr-rich phases that are found locally are Sr-bearing epidote and clinzoisite. In parts of the groundmass and as inclusion trails in amphiboles occurs ultra-fine-grained graphite (Fig. 8E). Other accessory phases include allanite, apatite, bastnasite, monazite, quartz, zircon, and smectite.

6. Geochemical results

6.1. Banded iron formation

6.1.1. Major and trace elements

For the bulk geochemical samples (Table 3), the SiO₂ concentration constitute \sim 45–67 wt.% and the Fe₂O₃ concentration \sim 30–52

wt.% (Table 3). For the individual silica-band geochemical separates, the SiO₂ concentration ranges from \sim 70 wt.% at Slemom Lake and up to as high as 94 wt.% at Goose lake. For the individual iron bands, the minimum Fe₂O₃ concentration is found at Slemom Lake with \sim 63 wt.% and the highest is \sim 75 wt.% at Goose Lake. The average SiO₂ concentration in the iron bands is \sim 25.5 wt.% whereas the average Fe₂O₃ concentration in the silica bands is only 10.5 wt.%.

When comparing the Al₂O₃ (and TiO₂) concentration between the four localities the highest average abundance is found at Slemom Lake, with a steady decrease from Damoti to Point and then Goose (Fig. 9A). For Goose Lake samples, the Al₂O₃ content is generally higher (1.58 wt.%) for the iron bands and lowest (0.19 wt.%) for the silica bands. This pattern is reversed in the Slemom Lake samples, where the silica band contains \sim 5.4 wt.% Al₂O₃ and the iron band only \sim 2.2 wt.% in the iron band (Table 3).

The high-field-strength elements (HFSE; Zr, Th, Sc and Hf) are all in relatively low concentrations (e.g., average of \sim 6 ppm Zr and \sim 0.4 ppm Th, Table 3) with the exception of the Slemom Lake samples, which have on average \sim 18 ppm Zr and \sim 1.4 ppm Th. In general, Al₂O₃ is well-correlated with these immobile elements (e.g., Fig. 9B) and relative more scatter exists between Al₂O₃ and Σ REE (Fig. 9C). The transition metals (e.g., Ni, Cr, V, Sc) are in general positively correlated (e.g., Sc vs. Ni; Fig. 9D). For the majority of the samples, the Cr content varies between 15–45 ppm; Cr is below the lower detection limit (0.5 ppm) for the Goose Lake silica bands (Table 3). A strong co-variation is evident between the transition metals and immobile HFSE (e.g., Sc vs. Th; Fig. 9E).

6.1.2. Rare earth elements and yttrium

The North American Shale Composite-normalized rare earth elements and yttrium pattern (REY_{NASC}; Gromet et al., 1984) for the four BIF locations are characterized by HREE enrichment relative to both MREE (Sm/Yb_{NASC} = 0.33–0.99) and LREE (Pr/Yb_{NASC} = 0.26–0.89, Fig. 11A). When normalizing to local shale (DGS = Damoti and Goose Shale), the HREE enrichment is even higher than when normalizing to NASC (Fig. 11A). In all the samples there are well-defined Eu anomalies (Eu/Eu_{NASC} = 1.24–3.4; average 1.92) and superchondritic Y anomalies (average Y/Ho = 36; Fig. 10A–D; Table 3). In general, the higher the Eu anomaly, the lower the total REY abundance (Fig. 10C and D).

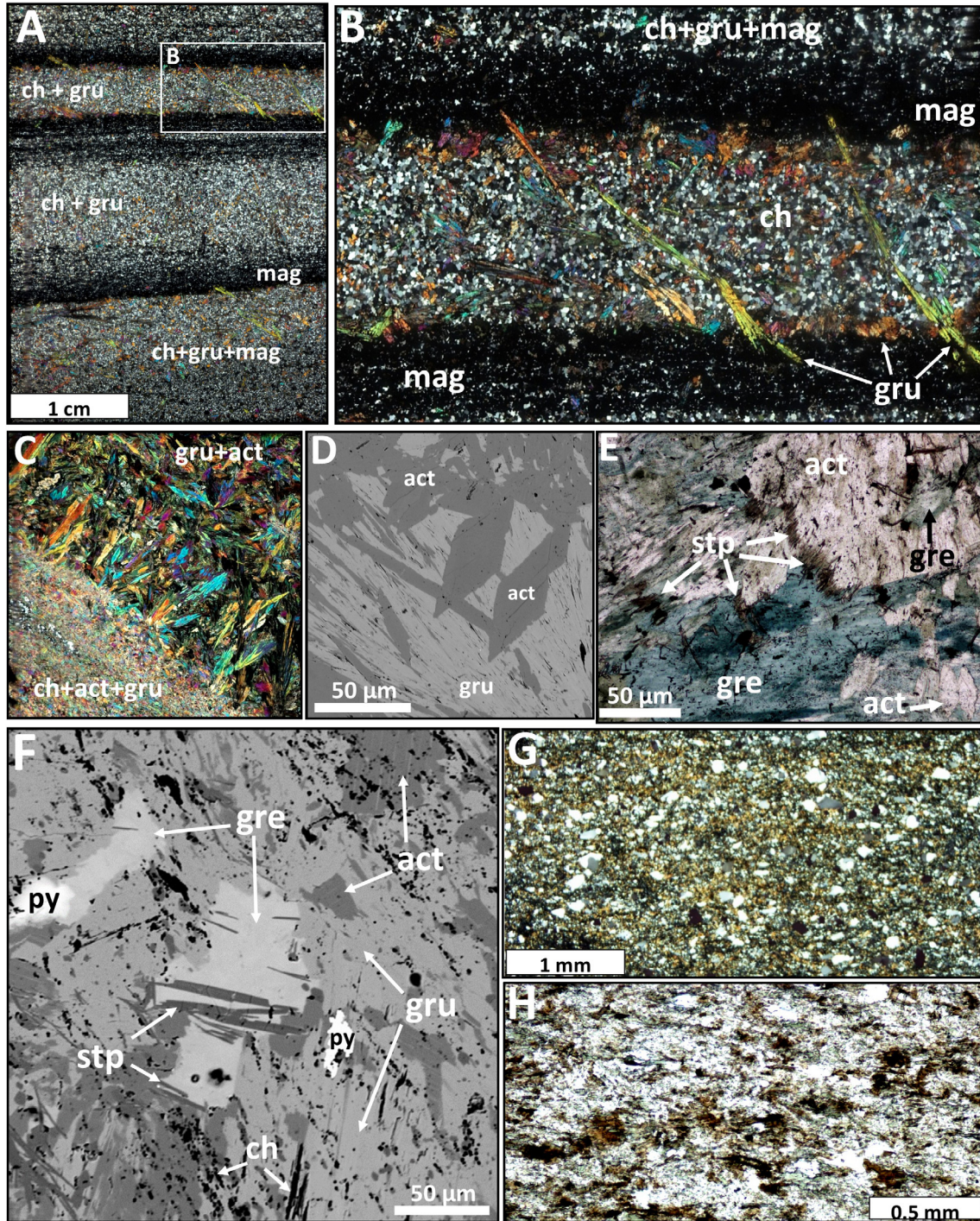


Fig. 7. (A, B) Photomicrographs of the Damoti Lake BIF showing large grunerite crystals cross-cutting the original bedding planes (in crossed polarized light = CPL). (C) Goose Lake BIF showing a mixture of chert, grunerite, and ferro-actinolite (CPL). (D) Electron microprobe backscatter image of (C) showing euhedral, diamond-shaped ferro-actinolite and radiating grunerite. (E) Goose Lake BIF showing ferro-actinolite with small bladed brown stilpnomelane on the edges and with large anhedral patches of greenalite (plane-polarized light = PPL). The stilpnomelane grows mostly within, or associated with, greenalite. (G) The ash tuff bed at Slemom Lake showing randomly distributed quartz fragments set in a very fine-grained groundmass of quartz, biotite, and chlorite (CPL). (H) PPL image showing the large amount of green chlorite.

The individual layers from the Slemom Lake BIF samples have the highest ΣREE (35–43 ppm) and elevated REY_{NASC} pattern, relative to the other locations studied (Fig. 10A, Table 3). The highest ΣREE content at Goose Lake occurs in the iron bands (average of 30 ppm), whereas the typical ΣREE in the silica bands is 4.7 ppm (Fig. 10D, Table 3). The REY_{NASC} LREE patterns are generally

concave-up (Fig. 10A–D) with distinct positive La anomalies (the combination of $\text{Pr}/\text{Pr}^* \sim 1$ and $\text{Ce}/\text{Ce}^* < 1$; Fig. 11B; Bau and Dulski, 1996). Four samples from Goose Lake (two iron bands, one silica band and one bulk BIF), one sample from Damoti Lake, and one from Point Lake, all exhibit clear negative Ce anomalies ($\text{Pr}/\text{Pr}^* > 1.05$; Fig. 11B).

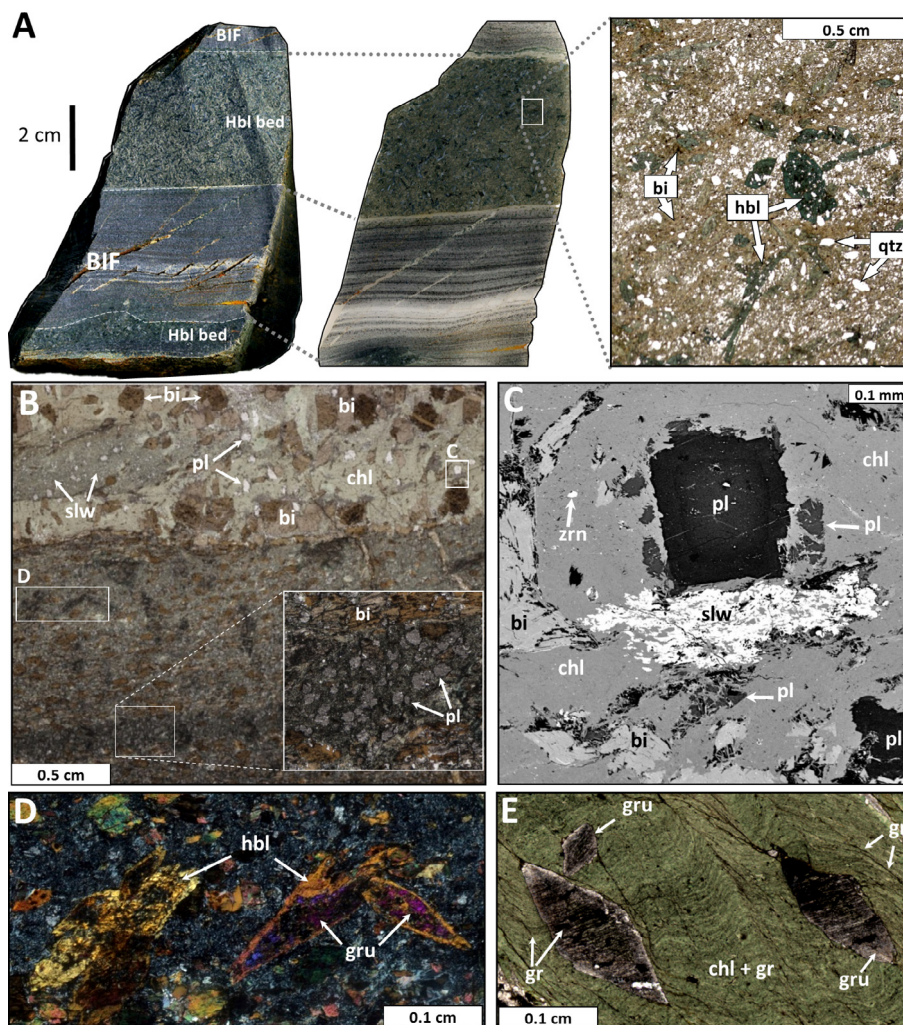


Fig. 8. (A) Hand sample, large thin section, and microphotos (in PPL) of the ferruginous beds at Point Lake (see Fig. 3E). The bed contains large ferro-hornblende porphyroblasts and quartz fragments that are randomly distributed in a biotite groundmass. Note the ferruginous bed and the BIF are repetitive on the scale of the hand sample. (B) Photo-micrograph (in PPL) of the ferruginous sediment at Damoti Lake. The sediment is texturally heterogeneous with variable grain sizes, in particular for the biotite porphyroblasts. Many of the plagioclase grains range from angular to sub-spherical. The lower half of the image has a darker appearance due to the abundance of ultrafine-grained graphite in the groundmass. (C) Detailed electron-microprobe backscatter image showing the relationship between angular plagioclase and the Sr-plagioclase (slawsonite). (D) Ferro-hornblende exists as crystals and as rims on existing grunerite (CPL). (E) Ferruginous bed with grunerite porphyroblasts set in a crenulated chlorite and graphite groundmass (PPL). The ultrafine graphite also appears as inclusion trails within grunerite crystals. Qtz = quartz, bi = biotite, hbl = hornblende, pl = plagioclase, chl = chlorite, slw = slawsonite, zrn = zircon, gru = grunerite, gr = graphite.

6.2. Tuff and turbidites

6.2.1. Tuff

The tuff bed at Slemon Lake (Table 4) contains high Al_2O_3 (23–24 wt.%) and relatively high loss on ignition (LOI; 3 wt.%; Table 4). The relatively immobile elemental HFSE ratios indicate the tuff is best classified as rhyodacite-dacite (Fig. 12A) and plots in the field of volcanic arc and syn-collision granites (Fig. 12B). The chondrite-normalized REE pattern of the tuff (Fig. 12C) demonstrates a LREE-to-HREE enriched REE pattern ($\text{La}_{\text{CH}}/\text{Yb}_{\text{CH}} \sim 8$). The tuff has a weak, but distinctly positive Eu anomaly ($\text{Eu}/\text{Eu}^* = 1.16$; Fig. 12C) and has positive anomalies of Th, Zr, Eu, and Y and negative Nb, P and Ti anomalies (Fig. 12D).

6.2.2. Turbidites – greywacke, mudstone, and ferruginous beds

The three greywacke samples analyzed in this study (Table 4) are characterized by low SiO_2 concentration but high Al_2O_3 , Fe_2O_3 and MgO relative to more mature sandstones. The chemical immaturity of the greywacke is further indicated by the $\text{Al}_2\text{O}_3/\text{Na}_2\text{O}$ ratio of ~ 4.8 , which is lower than for average sandstones (e.g., Henderson, 1975; Corcoran and Mueller, 2002). The $\text{Na}_2\text{O}/$

K_2O ratio for all the turbidites (greywacke, mudstone, and ferruginous beds) is ≤ 1 with the highest ratio in the greywackes.

The two mudstone samples have less SiO_2 and more TiO_2 , Fe_2O_3 , MgO, trace metals and LOI than the greywackes (Table 4). The ferruginous beds have less SiO_2 but a higher Fe_2O_3 content than the mudstone samples. All samples have close to similar $\text{Al}_2\text{O}_3/\text{TiO}_2$ ratios of ~ 25 (Table 4). The field and petrographic observations and the relatively high LOI in the mudstone and ferruginous beds are consistent with high organic content, now preserved as graphite. This has also been supported by X-ray diffraction analysis by Waychison (2011) who showed that the ferruginous sediment at Damoti Lake contains up to 13.5 wt.% graphite.

7. Discussion

7.1. Greenalite and stilpnomelane – retrograde metamorphism and the impact on the REY

Greenalite and stilpnomelane in BIF have been reported to form during late-diagenesis and very low-grade metamorphism

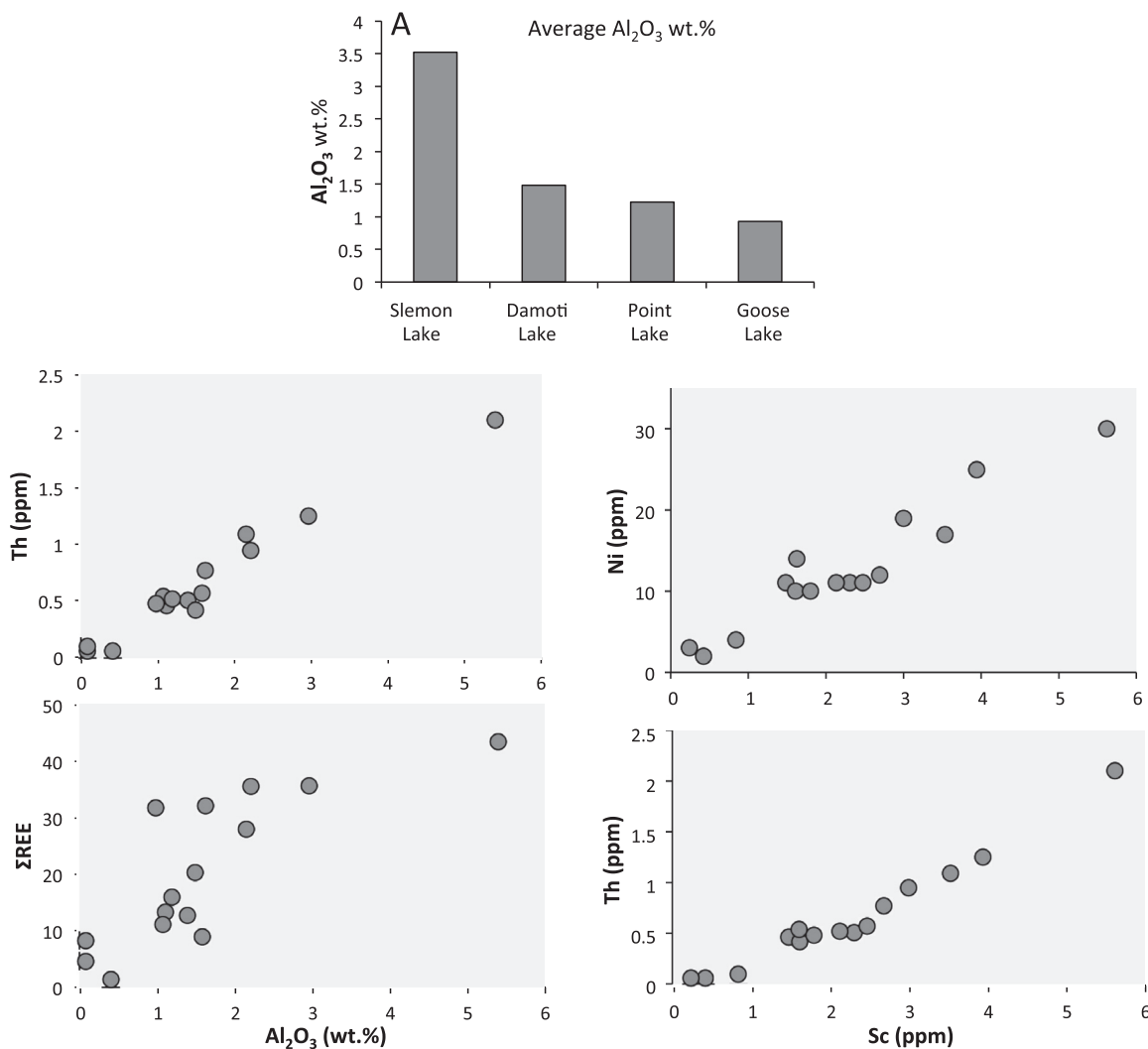


Fig. 9. Binary elemental plots of selected elements in the BIF. (A) The Slemon Lake BIF contains the largest amount of detrital material among the studied samples as recognized by its Al_2O_3 content. Only Goose Lake BIF has an Al_2O_3 content ≤ 1 wt.%. (B) The Al_2O_3 vs. Th showing a well-constrained positive correlation. (C) The Al_2O_3 vs. ΣREE showing a scattered relationship with only a weak linear correlation. (D, E) Both Th and Ni display a positive co-variation when plotted against Sc.

(<300 °C, Gole, 1980a) along with minnesotaite and siderite (Klein, 2005). Texturally, these low-grade phyllosilicates occur often as tiny microgranules and are proposed to have formed on the seafloor prior to burial of the BIF sediment (e.g., Rasmussen et al., 2013; Haugaard et al., 2016a; Tosca et al., 2016). Greenalite and stilpnomelane (such as in the Goose Lake BIF), can also form as a result of retrograde metamorphism, similar in origin to that reported from Neoproterozoic BIF within the Yilgarn craton (Gole, 1980b). This further highlights the complex origin of greenalite and stilpnomelane in BIF. The gold mineralization at Goose Lake has left an impact on the BIF geochemistry (Table 3), with higher sulfur content as a result of sulfide mineralization. Up to 1 wt.% chlorite (Cl) occurs in the greenalite and stilpnomelane (Table 2), supporting the secondary origin of these hydrous phyllosilicates. The impact on the REY from these syn- to post-metamorphic fluids will potentially be strong proximal to the fluid source as reported by Bau (1993). Pervasive fluid-rock interaction with reducing and high-temperature fluids will desorb the larger ionic radius of Eu^{2+} generating negative Eu anomalies in the BIF. Secondary phases like greenalite and stilpnomelane will discriminate against the larger Eu^{2+} ion in their crystal lattice leaving the BIF Eu-depleted. Furthermore, pervasive hydrothermal fluids will precipi-

tate quartz and carbonates in veins and fractures increasing the LREE content and lower the overall Eu/Sm ratio (Bau, 1993). These REY features, however, are not evident for the samples in this study (Fig. 10) and demonstrate the closed-system condition for the REY during various post-depositional processes. Another process that can impact the REY of BIF is during diagenesis. During diagenesis, the water-to-rock ratio is relatively high and can affect the distribution of REY among individual bands. Thus, Bau (1993) concluded that REY mobility during diagenesis would lead to a homogenization of the REY pattern between individual quartz- and iron-bands. In this study, each individual layer (Fig. 10A and D) shows variable REY pattern and therefore retained its specific REY signature through diagenesis.

7.2. The Neoproterozoic seawater composition

7.2.1. Lanthanum, cerium and the REY fractionation

In order to facilitate comparison between different chemical sediments around the world the REY in BIF is commonly normalized to one either the PAAS (post-Archaean Australian shale; Taylor and McLennan, 1985a) or the NASC (North American Shale Composite; Gromet et al., 1984).

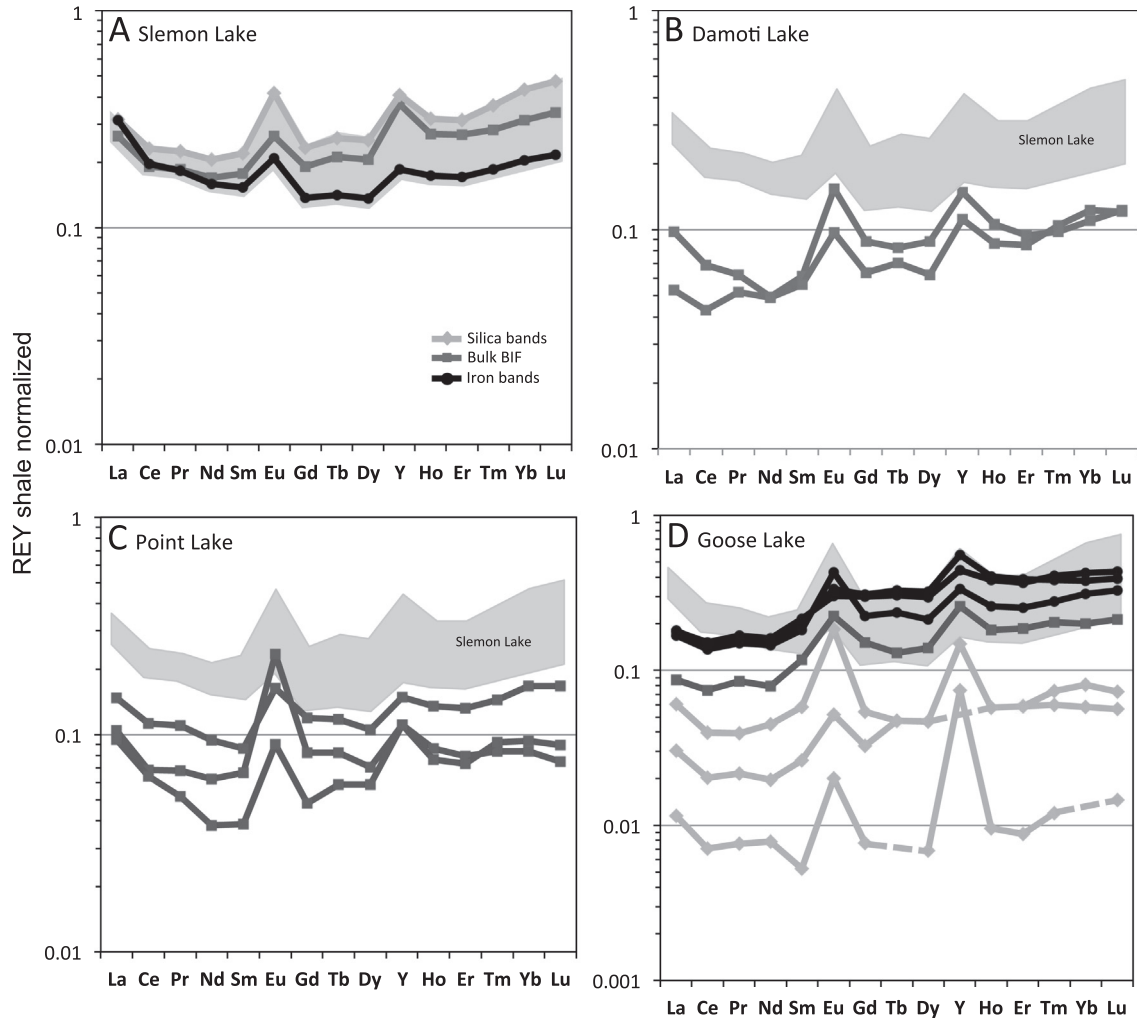


Fig. 10. The shale-normalized REY systematics of the BIF. In general, all samples have positive La, Eu, and Y anomalies. (A) Slemon Lake samples, including one bulk, one silica band, and one iron band, all show relatively high abundance of REY. Note the higher REY content in the silica band relative to the iron band. Despite the higher abundances the REY patterns are still HREE enriched. (B) Damoti Lake and (C) Point Lake BIF samples. Relative to Slemon Lake samples, these locations have lower REY content. (D) The iron bands at Goose Lake contain the highest amount of REY relative to the silica bands, contrary to the results from Slemon Lake. Note that the REY abundance in the iron bands is, however, comparable to Slemon Lake. Dashed connection lines = below detection limit. NASC normalization values from McLennan (1989).

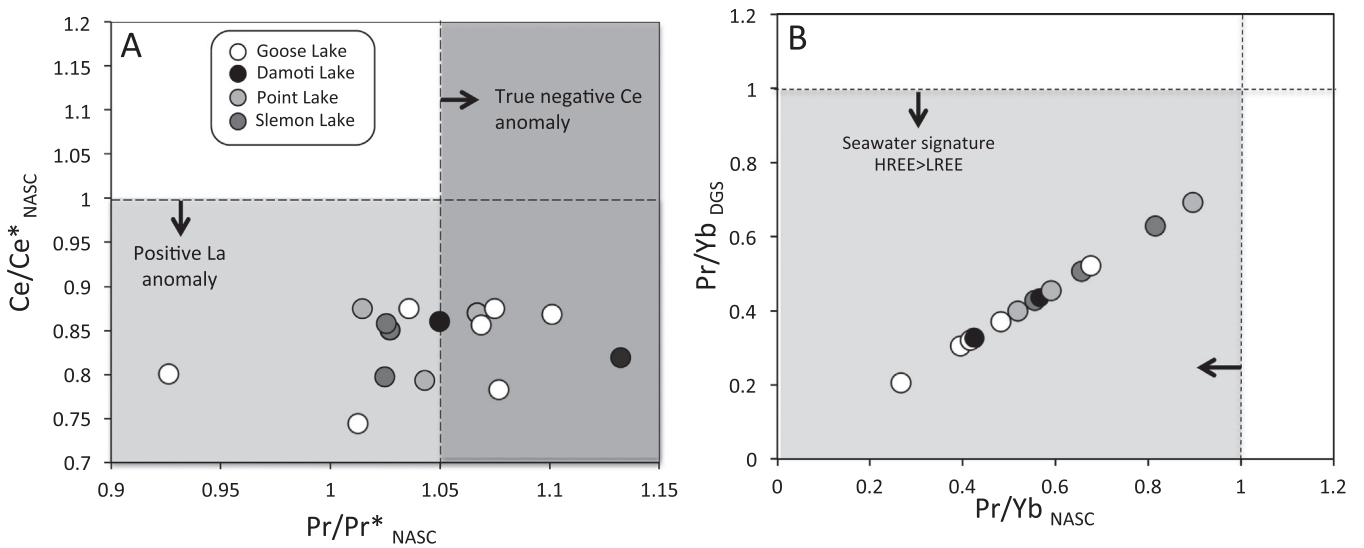


Fig. 11. (A) The quantitative depletion/enrichment of La and Ce in the BIF expressed as Pr/Pr^*_{NASC} versus Ce/Ce^*_{NASC} . Most samples plot in the field of positive La anomaly with no Ce anomaly (modified from Bau and Dulski, 1996). Six of the BIF samples plot within the field of negative cerium anomalies ($(Pr/Pr^*)_{NASC} > 1.05$). (B) Pr/Yb_{DGS} versus Pr/Yb_{NASC} (local shale DGS = Damoti and Goose Shale) diagram. Note the Pr/Yb is always below 1 but the fractionation is more pronounced when normalizing after DGS. See text for further explanations.

Table 4
Selected major and trace elements of the turbidite sediments associated with the BIF.

Lithology		Tuff bed	Greywacke	–	–	Mudstone	–	Ferruginous sediment	–	–	–
Location		Slemon Lake	–	Point Lake	Goose Lake	Damoti Lake	Goose Lake	Damoti Lake	–	–	Point Lake
Sample		RH-chisel	RHNWT-9A	RHNWT-29A	RH18140	RHNWT-20	RH36155	RHNWT-21	RHNWT-23A	RHNWT-23B	RHNWT-29C-2
Element (wt.%)	D.L.										
SiO ₂	0.01	54.08	67.25	65.99	72.19	50.82	59.44	51.81	45.6	49.46	48.9
Al ₂ O ₃	0.01	23.44	12.78	13.18	13.42	12.65	14.12	7.19	13.89	13.1	11.8
Fe ₂ O ₃ (t)	0.01	6.64	9	9.21	3.69	23.86	14.37	33.79	25.93	24.82	23.44
TiO ₂	0.001	0.49	0.51	0.52	0.42	0.67	0.59	0.39	0.60	0.67	0.52
MgO	0.01	2.8	2.21	2.5	1.47	4.82	2.86	2.99	4.88	5.09	4.73
CaO	0.01	0.84	1.31	1.55	1.63	0.11	0.75	2.63	1.52	0.62	5.66
Na ₂ O	0.01	3.54	3.04	2.5	2.69	<0.01	0.26	0.34	0.65	0.07	0.59
K ₂ O	0.01	5.17	2.91	3.21	3.2	0.03	4.15	1.24	2.53	0.92	2.61
MnO	0.001	0.029	0.026	0.033	0.042	0.068	0.04	0.054	0.067	0.072	0.1
P ₂ O ₅	0.01	0.15	0.1	0.1	0.07	0.09	0.07	0.07	0.05	0.1	0.15
LOI		2.96	0.92	0.89	0.91	5.81	3.66	0.27	4.15	5.4	1.22
Total	0.01	100.1	100.1	99.68	99.78	98.92	100.3	100.8	99.87	100.3	99.71
Zr (ppm)	1	202	136	103	105	78	99	60	149	96	113
Nb	0.2	10.7	5	3.4	5.50	5.4	5	3	8	6	4.4
Th	0.05	21.8	11	5.97	7.02	7.05	9.9	3.7	13.3	6.6	5.44
Hf	0.1	6.3	3.1	2.6	2.98	2.2	2.4	1.4	3.8	2.2	2.9
U	0.01	6.83	3.4	1.95	2.15	2.28	2.6	0.9	3.3	2.2	1.46
Ta	0.01	2.32	1.8	1.71	0.65	0.96	1.3	1.2	1.2	0.9	1.11
Sr	2	319	833	377	299	9	191	95	2494	422	31
Rb	1	154	114	113	134	3	185	103	208	77	110
Y	1	19	11	12	9.21	7	11	8	18	11	5
Sc	0.01	9.5	11	11.9	–	16.3	17	13	18	18	11.6
Cr	0.5	44.3	120	148	105	141	120	80	120	120	129
Ni	1	46	50	63	43.1	74	70	50	70	60	53
V	5	70	85	89	66.5	121	124	86	121	138	88
Ge	0.5	2	2	1.1	–	2	3	4	5	4	2.7
S (%)	0.001	0.005		0.004	–	0.005					0.01
La	0.05	16.9	25	21.4	22.1	21	23.5	13.1	34.4	20.2	18.4
Ce	0.05	37.1	50.4	46.2	50.7	41.4	45.2	28.4	72.1	40.8	37.8
Pr	0.01	4.37	5.63	5.27	5.80	4.49	5.16	3.61	8.83	4.87	4.4
Nd	0.05	17.3	20.6	19.6	21.5	16.6	19	15	32.4	17.6	17.6
Sm	0.01	3.81	3.5	3.67	3.69	3.3	3.3	2.9	5.7	3.1	3.22
Eu	0.005	1.48	0.76	1	1.11	1.26	1	1.1	1.83	1.31	1.13
Gd	0.01	3.24	2.7	2.85	2.91	2.83	2.6	2.3	4	2.4	2.63
Tb	0.01	0.49	0.4	0.42	0.33	0.44	0.4	0.3	0.6	0.4	0.37
Dy	0.01	2.88	2.2	2.28	1.83	2.71	2.2	1.7	3.6	2.1	1.95
Ho	0.01	0.56	0.4	0.41	0.35	0.54	0.5	0.3	0.7	0.4	0.38
Er	0.01	1.61	1.3	1.19	1.02	1.55	1.4	1	2.1	1.2	1.05
Tm	0.005	0.24	0.20	0.17	0.14	0.23	0.20	0.15	0.30	0.19	0.15
Yb	0.01	1.51	1.40	1.16	0.92	1.52	1.40	1.10	2.00	1.30	1.01
Lu	0.002	0.24	0.21	0.17	0.13	0.22	0.21	0.17	0.30	0.18	0.17

Dark grey = Fe bands, light grey = bulk BIF, white = silica bands; D.L. = detection limit.

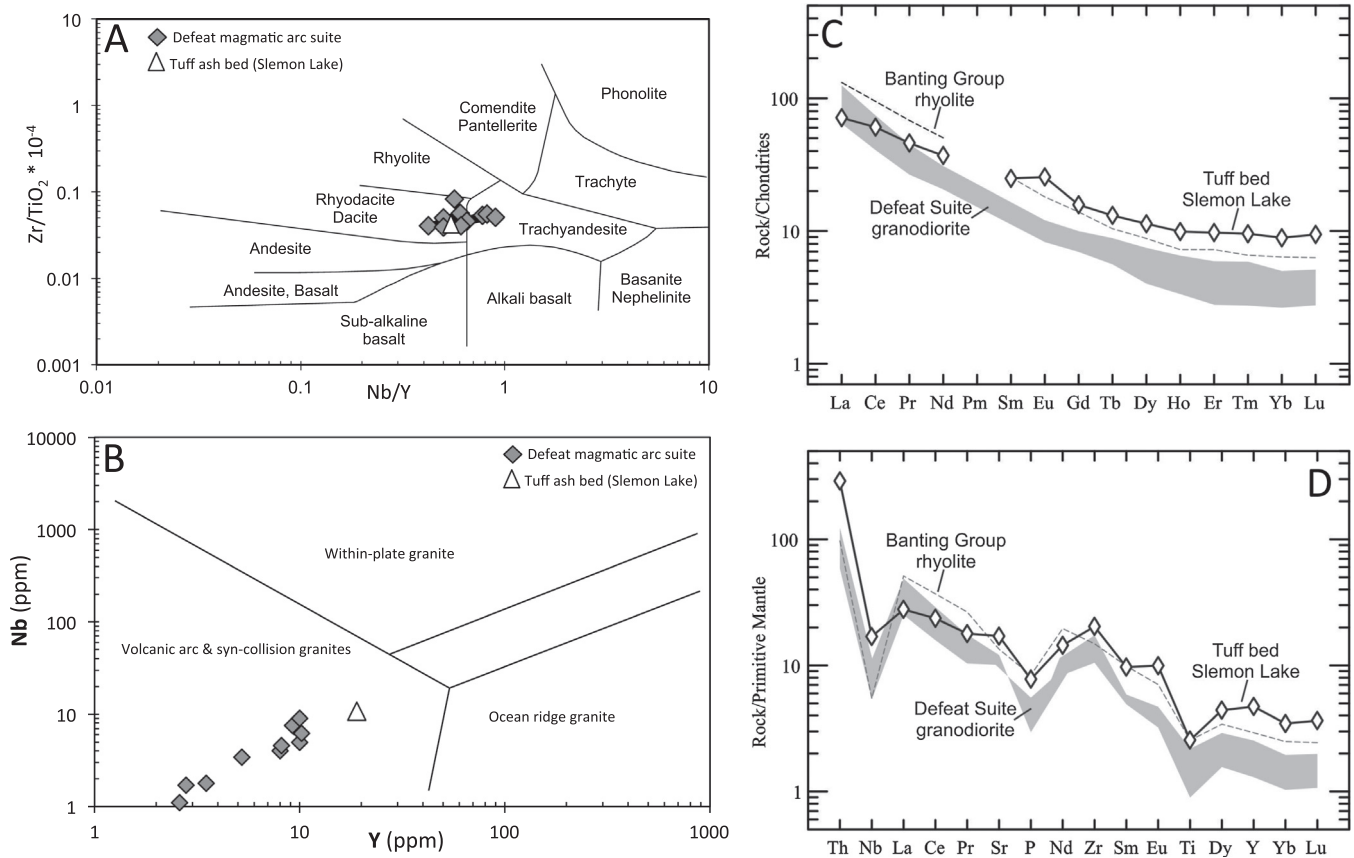


Fig. 12. (A) Geochemical classification diagram (Winchester and Floyd, 1977) for the tuff bed at Slemon Lake. The tuff bed is classified as a rhyodacite-dacite and is geochemically similar to the coeval Defeat magmatic arc rocks (data from Meintzer, 1987 and Yamashita et al., 1999). (B) Tectonic discrimination diagram from Pearce et al. (1984) showing the preferred setting for the tuff bed. (C) The chondrite-normalized REE pattern of the tuff bed at Slemon Lake, which is HREE enriched and shows a weakly developed Eu anomaly relative to both the contemporaneous Defeat magmatic suite and the older Banting Group rhyolites (normalization values after Anders and Grevesse, 1989). (D) Trace element diagram of the tuff bed at Slemon Lake displaying enrichment in HREE, Th, Y and Zr. Negative anomalies are found for Nb, P and Ti (normalization values after Sun and McDonough, 1989).

The Neoarchaean BIFs contain positive La anomalies as seen in Fig. 11. In marine water, La is stabilized in solution relative to neighboring REEs due to the absence of electrons in the inner 4f shell (e.g., De Baar et al., 1985). The positive La anomaly, therefore, suggests that La has been stabilized and weakly fractionated relative to the other LREE in the seawater column prior to precipitation. Six BIF samples also have negative Ce anomalies (see Fig. 11), which tends to indicate that a strong oxidant (e.g., O_2) was present in seawater that could oxidize Ce^{3+} to Ce^{4+} , thus leaving the local water column deficient in Ce because Ce^{4+} preferentially binds to Fe and Mn oxyhydroxides (e.g., Sholkovitz et al., 1994). This, of course, necessitates that the oxidation of Ce^{3+} took place away from the actual precipitation area.

The NASC-normalized REY patterns display Pr/Yb ratios < 1, which we interpret as being seawater of origin (Fig. 13). The evolution of the post-Archaean upper crust (as a whole) has largely been reconstructed through the chemistry of shales because their overall composition largely represents the erosion of the upper continental crust (e.g., Taylor and McLennan, 1985b, 2009). When addressing the REY pattern, normalization to local shale, however, may be more relevant as it is more contextually related to the depositional environment of the BIF. The contemporaneous local crust during the deposition of the BIF can be considered as the Damoti and Goose lakes shales (DGS). When normalizing the BIF samples after DGS, the REY fractionation (Pr/Yb_{DGS}) is constantly lower (higher HREE-to-LREE) compared to the NASC normalized Pr/Yb_{NASC} (Fig. 13), suggesting that the ambient seawater clearly fractionated the REY prior to BIF precipitation. The fractionation

likely originates from the fact that the HREE tends to stay longer in solution than the LREE, which will preferentially be adsorbed to particle surfaces (e.g., clay, organic matter) and thus becomes removed from solution (e.g., Cantrell and Byrne, 1987; Sholkovitz et al., 1994). A relative high input of fine-grained detrital material is recorded, particularly for the Slemon Lake samples, making them less suitable for detecting the seawater REY chemistry. However, on closer inspection, despite the up to 5.4 wt.% Al_2O_3 and the largest ΣREE of all BIF samples in this study, the Slemon Lake silica bands still have a lower Pr/Yb_{NASC} or Pr/Yb_{DGS} ratio than both the iron band and the bulk BIF (Fig. 10A). This, along with its positive La- and Y-anomalies, demonstrate that despite a relative large detrital input, the seawater can still influence the REY pattern, perhaps due to a high degree of adsorption between the fine-grained detritus and the ion-complexes in the ocean water.

7.2.2. Seawater Y/Ho and hydrothermal Eu/Sm

In the BIF, two of the most pronounced seawater REY signatures are superchondritic Y/Ho (>28) and positive Eu/Eu* (Fig. 10). Due to lower particle reactivity modern seawater holds Y longer in solution than Ho, increasing Y/Ho ratio in the ambient seawater (Bau and Dulski, 1999; Bolhar et al., 2004). The excess of Eu (as reduced Eu^{2+}) originates from high-T (>350 °C) hydrothermal fluids that circulate through submarine mafic crust along mid-ocean ridges (Danielson et al., 1992). The relative contribution from hydrothermal fluids to seawater composition can therefore be viewed through the elemental ratio of Eu/Sm (e.g., Alexander et al.,

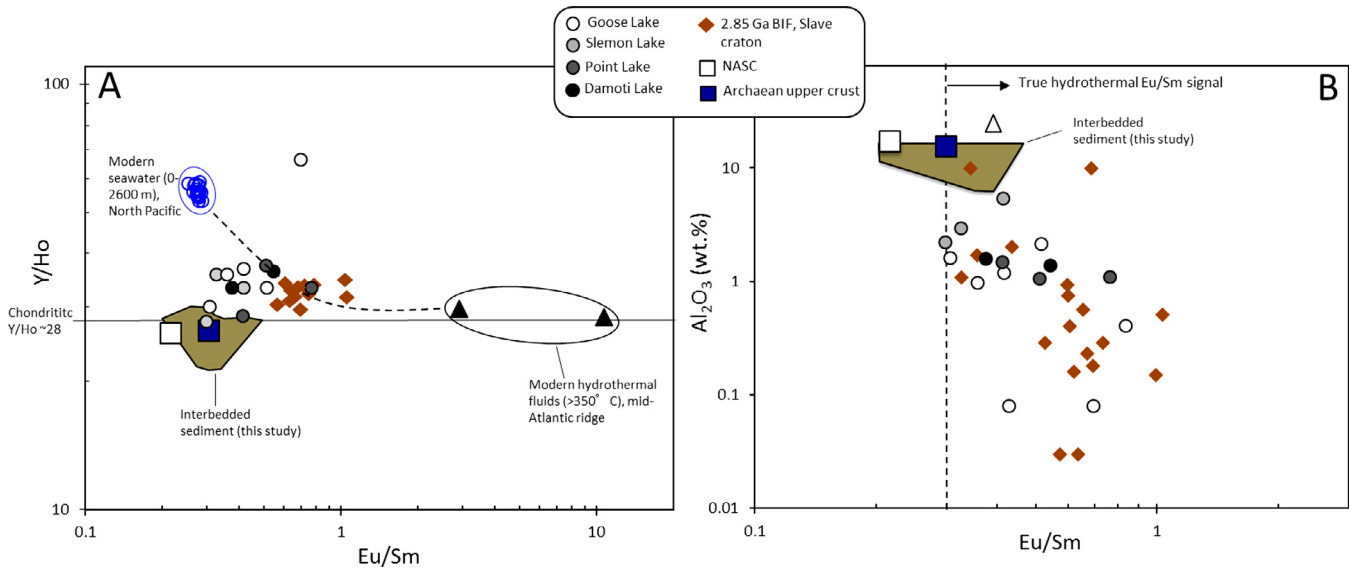


Fig. 13. (A) Elemental Eu/Sm versus Y/Ho showing the dominant sources for the BIF. Relative to the modern seawater, the BIF can be characterized as a mixture between seawater, hydrothermal fluids and a small detrital input controlled by the composition of the turbidite sediment. Note that the seawater input is higher and the hydrothermal input is lower in these Neoproterozoic BIF than for the Mesoarchean Slave craton BIF. (B) Elemental Eu/Sm versus Al_2O_3 illustrating the detrital impact on the BIF. A hydrothermal contribution to the BIF (and associated sediments) is indicated by a higher than Archaean crust value of ~ 0.3 . See text for further explanation. Modern hydrothermal fluids are from Bau and Dulski (1999); modern seawater data are Alibo and Nozaki (1999), and Slave craton 2.85 Ga BIF from Haugaard et al. (2016b).

2008). Using modern reservoirs like the upper seawater and hydrothermal fluids (Fig. 13A and B) reveals a complex depositional pattern behind the BIF samples. In the BIF, small amount of detrital material alongside the hydrothermal sources likely suppressed the superchondritic Y/Ho that is characteristic of the upper seawater (Fig. 13A). Relative to NASC, all BIF samples are skewed towards higher Eu/Sm ratios, which points towards a higher Eu/Sm contribution from injected hydrothermal fluids (Fig. 13B). However, looking closer in Fig. 13A, a large portion of the BIF samples Eu/Sm ratios similar to the associated clastic sedimentary rock sediment, which could point towards a degree of control on the Eu/Sm from the detrital material (note also that Archaean crust contains higher Eu/Sm than post-Archaean crust (NASC)). The clastic sediment that has higher Eu/Sm than the Archaean crust (>0.3) in this study is, specifically, the ferruginous sediment and the Fe-rich mudstones. These sediments have all obtained BIF components either from the water column during settling (Fe colloids adsorption, see also Section 7.3. below) or by erosion during active turbidite deposition. Therefore, the higher than Archaean crust Eu/Sm value of these sediments are likely due to the incorporation of BIF or precursor-BIF material (Fig. 13B) rather than being from the original source of the sediment. In support of this is that the three more felsic greywacke samples with no incorporated BIF components, all have Eu/Sm ratios below or at the Archaean crust value of ~ 0.3 (Table 4). Therefore the higher Eu/Sm ratios for both the BIF and associated Fe-rich sediment are likely of hydrothermal origin (Fig. 13B). This does not exclude that detrital input in the BIF can suppress the hydrothermal Eu/Sm signal. However, when looking at the Slemon Lake BIF and parts of the Goose Lake BIF (Fig. 13B), the highest Eu/Sm ratio is found in samples with highest Al_2O_3 and the one with the lowest Eu/Sm is found in BIF samples with lowest Al_2O_3 indicating that the size of the Eu/Sm ratio is dependent on the changes of the hydrothermal input to the seawater more than the amount of detrital material contaminating the BIF. It is noteworthy that the older Mesoarchean BIF in the Slave craton (Haugaard et al., 2016b) has an overall larger hydrothermal input than the Neoproterozoic BIF of the craton (Fig. 13A and B), where the younger BIF has overall higher seawater Y/Ho (Fig. 13A).

7.2.3. Hydrothermal versus continental weathering: Decoupling of iron and silica?

The source of iron and silica for Precambrian BIF has been a long-standing debate (e.g., Holland, 1973; Simonson, 1985; Dymek and Klein, 1988; Alibert and McCulloch, 1993; Rasmussen et al., 2015). It is now generally accepted that Fe^{2+} was sourced from mid-ocean hydrothermal activity and injected into anoxic bottom waters (e.g., Holland, 1973; Jacobsen and Pimental-Klose, 1988; Klein and Beukes, 1989; Polat and Frei, 2005; Frei and Polat, 2007). The Fe^{2+} was occasionally upwelled to the continental shelf, oxidized to Fe^{3+} by biological mechanisms (e.g., Pecoits et al., 2015), and subsequently precipitated as possible ferric oxyhydroxide, such as ferrihydrite. The provenance of silica, on the other hand, remains enigmatic since its origin has been linked to primary hydrothermal processes (Steinhofel et al., 2010), weathering of the surrounding landmasses (Hamade et al., 2003; Haugaard et al., 2016b), or incorporation via secondary fluids during post-depositional alteration (i.e., diagenesis; Rasmussen et al., 2015). Nevertheless, the work by Hamade et al. (2003), and later documented by Frei and Polat (2007), reveals that the siderophile element germanium (Ge), in conjunction with the silica content in BIF, can be used to characterize two interacting water masses during BIF precipitation. In many low-temperature processes the Ge/Si ratio does not fractionate as Ge and Si have similar atomic radii and bond lengths (Hamade et al., 2003 and references therein).

The Ge/Si molar ratio of present day mid-ocean hydrothermal fluids is between $\sim 8\text{--}14 \times 10^{-5}$ mol/mole (Mortlock et al., 1993), whereas the average continental crustal value is $\sim 0.13 \times 10^{-5}$ (Froelich, 1992). The Ge/Si of river waters, and hence the surface seawater, is strongly suppressed ($\sim 0.06 \times 10^{-5}$) since Ge uptake by land plants strongly fractionates the crustal Ge/Si ratio (Derry et al., 2005). However, on a plant-free Neoproterozoic Earth it is reasonable to assume that ambient upper seawater was close to the crustal Ge/Si value at the time. Silica and Fe are geochemically linked to Ge, where Ge has a positive co-variation with Fe and an inverse relation to Si content (Fig. 9F). The BIF samples in this study reveal a hyperbolic distribution of Si versus Ge/Si (Fig. 14A) that reflect mixing between hydrothermally controlled bottom water

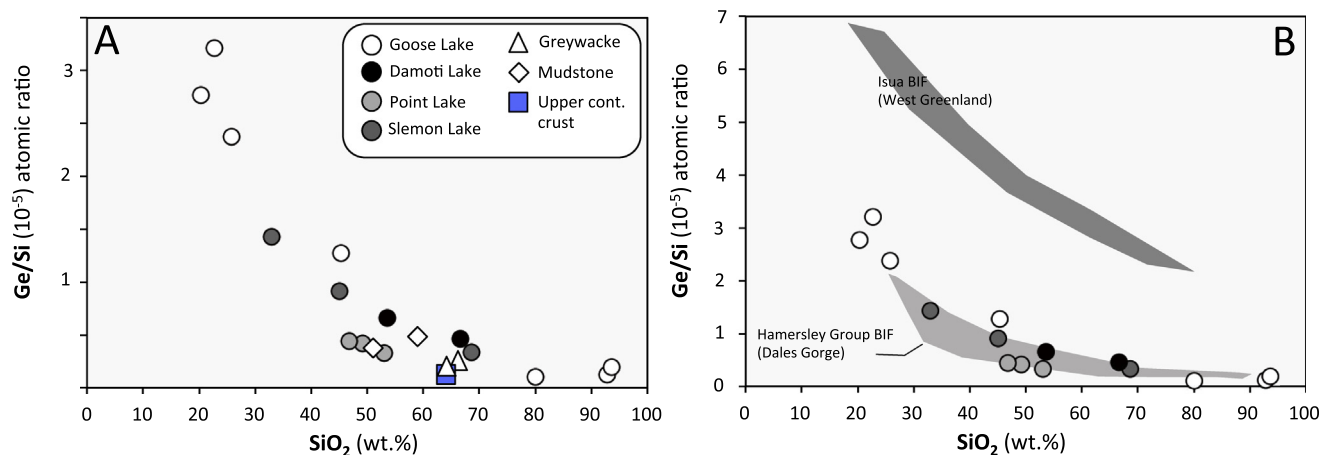


Fig. 14. The Ge/Si ratios in BIF. (A) A well-developed mixing-hyperbola characterizes the BIF sediment and potentially illustrates mixing between hydrothermally-controlled bottom water and continentally-controlled surface water. The Ge/Si ratio is high for the iron precipitate, whereas the Ge/Si values are low in the silica-rich BIF. (B) Same plot as (A) but with the Hamersley Group BIF (Hamade et al., 2003) and Isua BIF (Frei and Polat, 2007) added for comparison. A similar pattern is evident amongst all the three BIFs. The elevated Isua BIF is due to higher hydrothermal input into the bottom waters.

and continentally controlled surface water. Germanium concentrations are relatively high in hydrothermal fluids but will be scavenged by ferric oxyhydroxides during precipitation, relative to Si (Mortlock et al., 1993). Therefore, the Ge/Si will be higher than crustal values for bottom water and in a Fe^{3+} precipitate. If the Ge and Si remain unfractionated as reported by Hamade et al. (2003), the high Si content and low Ge/Si in BIF are best interpreted to represent the Ge/Si in ambient upper seawater. The mixing pattern between seafloor vented hydrothermal fluids and upper seawater (Fig. 14B), have also been demonstrated to exist within the 3.8 Ga Isua BIF (Frei and Polat, 2007) and the Palaeoproterozoic Dales Gorge BIF (Hamade et al., 2003). The Neoproterozoic BIF samples from the Slave craton plot within the same Ge/Si range as the Hamersley BIF, with the exception of three iron bands from Goose Lake. These have a higher Ge/Si signature, reminiscent of higher hydrothermal fluid input during deposition (Fig. 14B). The Ge/Si ratio in the Isua BIF is even higher, likely reflecting a larger Ge input due to the more vigorous submarine hydrothermal venting at that time (Fig. 14B; Frei and Polat, 2007).

The greywacke samples in this study show very low Ge/Si, closer to and typical of upper continental crustal values, whereas the mudstones have more elevated Ge/Si ($\sim 0.13 \times 10^{-5}$; Fig. 14A). As the mudstones represent slow settling of pelagic clay- and silt-particles from iron-rich seawater, they may have inherited a hydrothermal Ge/Si component. The extremely high SiO_2 content for some of the silica bands from Goose Lake (Fig. 14A) is also associated with the same Ge/Si ratio as the greywackes, demonstrating the usefulness of the Ge/Si system to infer the silica and iron source characteristics and the interaction of different water masses in the seawater.

7.3. The nature of the interbedded rocks

7.3.1. Active volcanism during BIF deposition

The presence of a tuffaceous bed within the deep-water turbidite-BIF sequence suggests that the depositional basin was temporally and spatially linked to felsic volcanism. The detrital zircon record of the turbidite-BIF sequence supports this, as the youngest zircons found in the associated greywackes have ages corresponding to the ca. 2635–2620 Ma Defeat Suite plutons (Ootes et al., 2009) that are preserved in a northeast-southwest striking belt across the southern part of the craton (e.g., Davis et al., 2003; Ootes et al., 2009). It is likely that the ca. 2620 Ma

ash tuff bed at Slemon Lake is derived by late stage volcanism related to this magmatic event (Haugaard et al., 2017).

Determining the source of a single ash tuff bed deposited in the Archaean marine environment is not without complications. Weathering, adsorption and leaching of elements during ash deposition through the water column may alter primary chemical attributes (e.g., Censi et al., 2007; Haugaard et al., 2016a). For example, the 23–24 wt.% Al_2O_3 in the tuff (Table 4) is likely a weathering phenomenon in the sense that other more mobile major elements were selectively leached away during rainout through the water column or during diagenetic compaction and interaction with pore waters. The volatile content (3 wt.% LOI) also supports that the bed was altered to some degree. As such, classifying the rock type with the major elements is considered suspect. Utilizing HFSE ratios, the tuff appears chemically similar to the Defeat Suite granodiorite plutons (Fig. 12A). The Defeat Suite are I-type plutons, and have elevated chondrite-normalized LREE and Th and pronounced negative Nb, P, and Ti anomalies analogous to those in modern magmas along active continental margins such as the Andes (Fig. 12B–D; Ootes et al., 2009). The tuff from Slemon Lake displays the same normalized pattern, supporting that the depositional basin for the BIF-turbidites may have been associated with a larger, convergent margin (arc?) type tectonic setting (Fig. 12B–D; Ootes et al., 2009). Caution should be taken, however, as this interpretation is only based on one single tuff bed. The REE and trace elements in Slemon Lake tuff bed are less fractionated than the Defeat Suite plutons and the older (ca. 2663 Ma) Banting Group rhyolites (Fig. 12C). This pattern could reflect that (1) the tuff's parental magma was of more intermediate character than the Defeat and Banting rocks, or (2) the fine-grained ash particles reacted with the ambient seawater during settling, thereby incorporate a portion of the seawater HREE by ion adsorption to reactive particle surfaces. Also the weakly elevated Eu anomaly (Fig. 12C) could potentially be inherited from the ambient hydrothermal enriched seawater rather than being a direct proxy of the magma source. The seawater-influence on the REY budget has similarly been demonstrated for tuffaceous beds within the Hamersley Group BIF, Western Australia (Haugaard et al., 2016a).

7.3.2. Turbidites – composition and sources

The provenance of detrital zircon in the ca. 2620 Ma turbidites indicates most of the detrital input from older volcanic rocks (ca. 2700–2660 Ma), with only a minor input of ca. 2620 Ma zircons

(Ootes et al., 2009; Haugaard et al., 2017); the dominant source for the greywackes being the older supracrustal rocks of the Slave craton (Fig. 1b). Studies of the older (~2661 Ma) Burwash turbidites by Jenner et al. (1981) and Yamashita and Creaser (1999), show that those greywacke turbidites can best be explained by a mixture of 55% felsic volcanic rocks, 25% granite and 20% mafic-to-intermediate volcanic rocks similar in proportion as what is exposed in the Yellowknife area of the craton. The geochemistry of the younger greywackes (~2620 Ma) shows that these also have contributions from both felsic and mafic sources. The higher SiO₂, elevated Na₂O/K₂O ratio (although still ≤ 1) and lower content of Fe₂O₃ and MgO (relative to the corresponding mudstone and ferruginous sediment) collectively imply that the greywackes contain more quartz and feldspar than fine argillaceous material of chlorite and mica. However, when comparing these to the older Burwash Formation, the latter have a reverse ratio of Na₂O/K₂O, with sodium content between 1.5 to 2 times its potassium content (Henderson, 1975; Yamashita and Creaser, 1999). A Na₂O/K₂O ratio >1 relates to a higher albite content of the feldspars in these turbidites whereas the low Na₂O/K₂O in the turbidites in our study reflect a higher K-feldspar component in the source terrain or a more extensive recycling of the sediment.

The compositionally heterogeneous ferruginous bed has a higher content of mafic minerals with lower SiO₂ and higher Fe₂O₃ and MgO contents than the greywacke. It is important to point out that the high Fe content may not be entirely due to the composition of the source material, but potentially a result of either interaction of the fine-grained detritus with the deep, iron-rich seawater prior to deposition, or the enrichment of iron through the submarine erosion of the underlying BIF sediment as reported above. At Point Lake, a large input of angular quartz, together with many detrital zircons, points towards a contribution from a felsic provenance at this location. In contrast, the angular detrital grains at Damoti Lake are dominated by plagioclase (Fig. 8B) that may have been derived from intermediate-to-mafic provenance.

To discriminate between different provenances of sediment, measurements of Th, La, and Sc have previously proved useful as Th and La are incompatible and Sc compatible during magmatic differentiation (e.g., Taylor and McLennan, 1985a). Scandium is highly compatible with clinopyroxene and, therefore, a good indicator of any mafic sources. Using those elements (Fig. 15A), the BIF-related turbidite sediments, together with the Burwash turbidites, plot as intermediate between mafic sources (best represented by the Kam and Banting group basalts) and felsic sources (Banting Group rhyolite and Defeat Suite granodiorite plutons; Yamashita and Creaser, 1999). In fact, the sediments are more mafic (lower Th/Sc and La/Sc) than the average upper crust of the Archaean. This is particularly the case for some of the mudstone and ferruginous beds (Fig. 15A).

7.3.3. The BIF-turbidite association

The presence of chemical sedimentary rocks (BIF) within a relatively large volume of greywacke-mudstone turbidites is intriguing because the two deposits represent significantly different styles of marine sedimentation. The BIF is characterized by a slow rainout of ferric oxyhydroxides and amorphous silica from low-energy seawater (below storm-wave base). The siliciclastic rocks represent dynamic and high-energy flow processes with depositional rates measured within days or even hours (e.g., Selley, 1988; Zane et al., 2012).

A slow background precipitation of the precursor components to BIF was periodically interrupted by influxes of clastic sediments sourced from distal-to-proximal submarine fans. These pulses of sediment occasionally eroded the top portion of the underlying BIF unit leaving both erosional scour marks on the BIF surface

(Fig. 3B) and producing intraformational mud rip-up clasts demonstrating the dynamic character of the sandy parts of the turbidites (see also Henderson, 1975).

Although different interpretations exist of deep-marine sedimentation for modern and ancient submarine fans (e.g., Nilsen, 1980), we interpret the thickest turbidites to have been deposited proximal to the source channel at the submarine fan beyond the continental slope or ramp. The thinner and finer-grained sequences then represent channel-distal deposition related to sediment lobes prograding further out into more quiet and deeper water. As such, the BIF-turbidite deposition was restricted to deeper waters associated with the basin plain. A possible analogue to the BIF-turbidites is in the Neoproterozoic Beardmore-Geraldton metasedimentary belt in the Superior craton. There, a large proportion of the sedimentary rocks contain oxide-facies BIF that are interbedded with turbidites (Barrett and Fralick, 1985, 1989). A model for that BIF-turbidite succession is a submarine interchannel setting (Barrett and Fralick, 1989). In interchannel areas, between feeder channels and fan development, BIF could have precipitated alongside repeated episodes of clastic input from channel spill-over during the progradation of turbidite currents (Barrett and Fralick, 1989). Although more sedimentologic work needs to be carried out on these interbedded deposits, it is evident that not all of the sandy greywackes are fining upwards (e.g., at Goose Lake). Instead, some display vertically unstructured packages with a homogenous grain size distribution (Fig. 5).

If the BIF-turbidites were deposited within a back-arc basin, as suggested by Ootes et al. (2009) and supported by this study, it is likely that the tectonically active arc-terrain would rapidly supply large amounts of sediments to the outer shelf through various distributary mouth bars. Subsequently, movement of this sediment could be triggered with gravity flows and slumps prograding down the continental slope, causing unsorted mass-flow deposits rather than true turbiditic deposits (e.g., Barrett and Fralick, 1989; Haugaard et al., 2013).

The nature of the more mafic ferruginous beds is not as straightforward. Field observations at Damoti Lake indicate both detrital magnetite grains and rip-up clasts of the underlying BIF within the ferruginous beds (Waychison, 2011). This, along with the soft-sediment deformation and scour marks of the BIF, suggests that the ferruginous beds were deposited by flow processes similar to the greywacke turbidites. At Point Lake, the sediment contains angular detrital quartz grains (Fig. 8A) and multi-sourced zircon crystals (see Haugaard et al., 2017 for detrital zircon distribution in this bed) as do the greywackes. As such, they represent the base of the turbidite that is intermixed with the underlying BIF. This would explain their high iron content (Table 4) and why these sediment beds are only found immediately adjacent to the BIF beds.

7.4. Detrital contribution to BIF deposition

Along with the hydrothermal and seawater signatures in the BIF, the high amount of clastic input to the basin impacted the chemical sedimentation, and as such, the overall chemistry of the BIF. For example, during precipitation of the Slemmon Lake BIF, fine-grained detritus was co-deposited and this led to higher Al₂O₃, TiO₂, Zr, Th, Nb, and to some degree, the REY. As a consequence, a higher modal content of secondary minerals such as chlorite and actinolite developed during later metamorphism.

The detrital impact on BIF precipitation can be assessed by the concentrations of Al₂O₃ and TiO₂. It is generally believed that they do not fractionate during weathering and transport within the sedimentary environment (e.g., Sugitani et al., 2006). Thus, the Al₂O₃/TiO₂ ratio in the detrital material deposited in the BIF basin would reflect the average Al₂O₃/TiO₂ ratio of the source detrital material. The BIF samples display a relatively constant intermediate Al₂O₃/

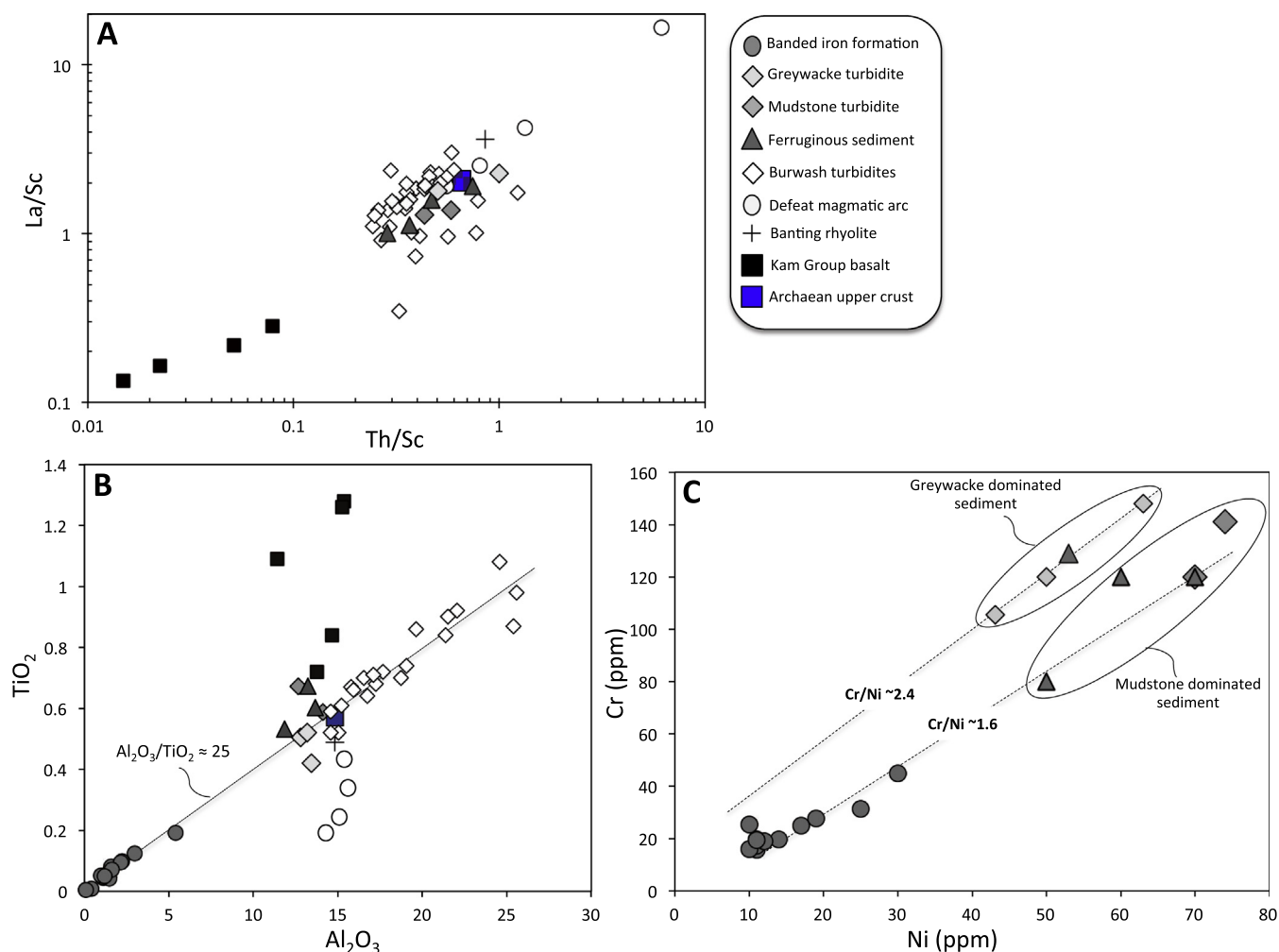


Fig. 15. (A) Th/Sc versus La/Sc diagram used to discriminate the influence from local mafic and felsic sources on the sediment budget. The turbiditic sediment resembles that of the Burwash greywacke sediment with a mixture of the Kam Group basalt and Banting/Defeat granodiorite detritus. Note that the sediment generally has higher Sc than the average Archaean upper crust. (B) The average Al₂O₃/TiO₂ ratio of the BIF (~25) is controlled by the provenance that also sourced the interbedded greywacke and mudstone sediment. The exception is the one mudstone and one ferruginous sediment from Damoti Lake, which both have lower Al₂O₃/TiO₂ ratios due to higher TiO₂ content contributed from mafic sources. (C) Trace metals in the BIF are controlled by the fine-grained mudstone and ferruginous sediment. With a Cr/Ni ratio of ~1.6 for the BIF and the mudstone and ferruginous sediment it is unlikely that Ni was preferentially enriched in the seawater prior to BIF precipitation. Kam Group basalt and Burwash sediment are from Yamashita and Creaser (1999); Defeat magmatic arc is from Meintzer (1987) and Yamashita et al. (1999). Archaean upper crust is from Taylor and McLennan (2009).

TiO₂ ratio of 25 (Fig. 15B). This correlates well with the interbedded greywacke, as well as the older Burwash turbidites reported by Yamashita and Creaser (1999) and, not surprisingly, it shows a dominant control on the detritus in the BIF from these units. Although they share the same Al₂O₃/TiO₂ ratios, the lower content of both Al₂O₃ and TiO₂ in the turbidites from this study, relative to the Burwash turbidites (Fig. 15B), probably reflects modal differences in the proportion of fine sand, silt and clay. Due to a higher mafic input, the mudstones from Damoti Lake have elevated concentrations of TiO₂ approaching some of the Kam Group basalts (Fig. 15B). The positive relationship between Th and Sc (Fig. 9E) also shows that the detritus in the BIF was delivered from already well-mixed sources, perhaps from resedimentation from submarine sediment lobes on the continental outer slope.

The trace metals Ni and Cr in the BIF are largely hosted by the fine-grained mudstone and ferruginous sediment facies, not by the greywacke sediment (Fig. 15C). The Cr-Ni trends for many BIF have been shown to be non-representative of the source that provided the detritus because, unlike Cr, Ni is more likely to go in solution and concentrated in the seawater and subsequently the BIF deposit (Konhauser et al., 2009). This lowers the overall

Cr/Ni ratio relative to the sources that provided those metals. In this study, the Cr/Ni of ~1.6 is significantly lower than the greywacke Cr/Ni of ~2.4 (Fig. 15C). However, the BIF Cr/Ni ratio seems to have been controlled by the finer-grained mudstone and ferruginous sediment and not by the ambient seawater. This control from clastic sources is not surprisingly since the BIF basin was significantly impacted by turbiditic sedimentation and this demonstrates that the impact of detrital sediment on BIF deposition can obscure the subtle signal of the seawater chemistry.

8. Conclusions

The Neoproterozoic (~2620 Ma) BIF of the Slave craton was deposited within one of the most extensive and well-preserved Archaean turbidite basins in the world. The BIF contains micro- and meso-bands of chert and magnetite, along with well-developed amphiboles (grunerite and ferro-actinolite) and minor retrograde greenschist and stilpnomelane. The BIF is intercalated with greywacke-mudstone turbidites, ferruginous beds, and in one example a felsic (dacitic) ash tuff.

On a layer-by-layer basis, there is relatively more silica in the iron bands than iron in the silica bands, a pattern that likely resulted from a continuous rainout of silica that was interrupted by pulses of iron-rich deep water circulation. The decoupled source of silica and iron during BIF deposition is supported by Ge/Si, with weathering of local landmasses supplying the silica to the surface waters, while hydrothermal fluids with higher Ge/Si supplied the deeper, hydrothermally-sourced iron-rich waters.

The high input of clastic sediment with the BIF, now preserved as greywacke, contaminated the chemical precipitates on various scales. The BIF has similar $\text{Al}_2\text{O}_3/\text{TiO}_2$ and Cr/Ni ratios as the turbidite sediment, illustrating the strong control from the latter on the element budget in the BIF. Despite this, the BIF still records some important seawater features such as a fractionated shale-normalized REY pattern with $\text{Pr}/\text{Yb} \ll 1$, and positive La and Y anomalies (average $\text{Y}/\text{Ho} = 36$). The hydrothermal contribution to the ambient seawater is recorded by a pronounced Eu anomaly whereas parts of the BIF exhibit negative Ce anomalies, indicating water column oxygenation was sufficient to fractionate Ce from neighboring REE.

The interbedded tuff bed at Slemmon Lake shows that the BIF deposition was associated with active volcanism presumably from the ca. 2635–2620 Ma Defeat magmatic arc. We propose that the most likely depositional scenario for the BIF is on the basin plain proximal to a steep continental slope. Here, turbidite currents and debris flows moved through submarine feeder channels, episodically interrupting the chemical rainout of ferric oxyhydroxides and amorphous silica.

Acknowledgements

This work benefitted greatly from the help of Martin Von Dollen and Mark Labbe in the thin section lab, pilot Samantha Melliott, and Sabina Gold and Silver Corp. (particularly Rachel Abbott, Francois Berniolles and Dave Smith) for transport, accommodation, and allowing us access to core samples. Lastly, a big thank you Andrew Locock at the University of Alberta electron microprobe facility for helping out with the chemical formulas of greenalite and stilpnomelane. Funding for this research was given by the Polar Continental Shelf Project (#65412) to RH and LO, the Natural Sciences and Engineering Research Council of Canada (NSERC) to KK, the Circumpolar/Boreal Alberta Research Grants (C/BAR) program of the CCI-Canadian Circumpolar Institute (Grant #CG428) to RH. This publication is NWT Geological Survey contribution #0099.

References

- Alexander, B.W., Bau, M., Andersson, P., Dulski, P., 2008. Continentally-derived solutes in shallow Archean seawater: rare earth element and Nd isotope evidence in iron formation from the 2.9 Ga Pongola Supergroup, South Africa. *Geochimica et Cosmochimica Acta* 72, 378–394.
- Alibert, C., McCulloch, M.T., 1993. Rare earth element and neodymium composition of the banded iron formations and associated shales from Hamersley, Western Australia. *Geochimica et Cosmochimica Acta* 57, 187–204.
- Alibo, D.S., Nozaki, Y., 1999. Rare earth elements in seawater: Particle association, shale-normalization, and Ce oxidation. *Geochim. Cosmochim. Acta* 63, 363–372.
- Anders, E., Grevesse, N., 1989. Abundances of the elements: meteoric and solar. *Geochim. Cosmochim. Acta* 53, 197–214.
- Barrett, T.J., Fralick, P.W., 1985. Sediment redeposition in Archean Iron Formation: Examples from the Beardmore-Geraldton Belt, Ontario. *J. Sediment. Petrol.* 55, 205–212.
- Barrett, T.J., Fralick, P.W., 1989. Turbidites and iron formations, Beardmore-Geraldton, Ontario: application of a combined ramp/fan model to Archean clastic and chemical sedimentation. *Sedimentology* 36, 221–234.
- Bau, M., 1993. Effects of syn- and post-depositional processes on the rare-earth element distribution in Precambrian iron-formations. *Eur. J. Mineral.* 5, 257–267.
- Bau, M., Dulski, P., 1996. Distribution of yttrium and rare-earth elements in the Penge and Kuruman iron-formations, Transvaal Supergroup, South Africa. *Precamb. Res.* 79, 37–55.
- Bau, M., Möller, P., 1993. Rare earth element systematics of the chemically precipitated component in Early Precambrian iron formations and the evolution of the terrestrial atmosphere–hydrosphere–lithosphere system. *Geochimica et Cosmochimica Acta* 57, 2239–2249.
- Bekker, A., Holland, H.D., 2012. Oxygen overshoot and recovery during the early Paleoproterozoic. *Earth Planet. Sci. Lett.* 317–318, 295–304.
- Bekker, A., Holland, H.D., Wang, P.-L., Rumble, D., Stein, H.J., Hannah, J.L., Coetzee, L.L., Beukes, N.J., 2004. Dating the rise of atmospheric oxygen. *Nature* 427, 117–120.
- Bekker, A., Slack, J.F., Planavsky, N., Krapež, B., Hofmann, A., Konhauser, K.O., Rouxel, O.J., 2010. Iron formation: the sedimentary product of a complex interplay among mantle, tectonic, oceanic, and biospheric processes. *Econ. Geol.* 105, 467–508.
- Bekker, A., Kasting, J., Anbar, A., 2013. Evolution of the atmosphere and ocean through time. *Chem. Geol.* 362, 1–2.
- Bekker, A., Planavsky, N.J., Krapež, B., Rasmussen, B., Hofmann, A., Slack, J.F., Rouxel, O.J., Konhauser, K.O., 2014. Iron formations: their origins and implications for ancient seawater chemistry. In: Reference Module in Earth Systems and Environmental Sciences. 2nd ed., Treatise on Geochemistry 2nd ed., vol. 9, pp. 561–628.
- Bennett, V., Jackson, V.A., Rivers, T., Relf, C., Horan, P., Tubrett, M., 2005. Geology and U–Pb geochronology of the Neoproterozoic Snare River terrane: tracking evolving tectonic regimes and crustal growth. *Can. J. Earth Sci.* 43, 895–934.
- Bleeker, W., 2002. Archean tectonics: a review, with illustrations from the Slave craton. In: Fowler, C.M.R., Ebinger, C.J., Hawkesworth, C.J. (Eds.), *The Early Earth: Physical, Chemical and Biological Development*, vol. 199. The Geological Society, London, pp. 151–181.
- Bleeker, W., Hall, B., 2007. The Slave Craton: Geological and Metallogenetic Evolution, in Goodfellow, W.D., ed., *Mineral Deposits of Canada: A synthesis of major Deposit-types, District Metallogeny, the evolution of geological provinces, and exploration methods*. Geological Society of Canada, Mineral deposit division, Special Publication 5, 849–879.
- Bleeker, W., Villeneuve, M.E., 1995. Structural studies along the Slave portion of the SNORCLE transect. In: Slave-northern cordillera lithospheric evolution (SNORCLE) transect and cordilleran tectonics workshop. F. Cook, P. Erdmer (Eds.). *Lithoprobe Report*, vol. 44, pp. 8–13.
- Bolhar, R., Kamber, B.S., Moorbath, S., Fedo, C.M., Whitehouse, M.J., 2004. Characterisation of early Archean chemical sediments by trace element signatures. *Earth Planet. Sci. Lett.* 222, 43–60.
- Bostock, H.H., 1980. Geology of the Itchen Lake area, District of Mackenzie. *Geol. Surv. Can. Mem.* 391, 101.
- Byrne, R.H., Kim, K.-H., 1990. Rare earth element scavenging in seawater. *Geochimica et Cosmochimica Acta* 54, 2645–2656.
- Cantrell, K.J., Byrne, J.H., 1987. Rare earth element complexation by carbonate and oxalate ions. *Geochimica et Cosmochimica Acta* 51, 597–605.
- Censi, P., Saiano, F., Mazzola, S., Ferla, P., 2007. Alteration effects of volcanic ash in seawater: anomalous Y/Ho ratios in coastal waters of the Central Mediterranean sea. *Geochimica et Cosmochimica Acta* 71, 5405–5422.
- Corcoran, P.L., Mueller, W.U., 2002. The effects of weathering, sorting and source composition in Archean high-relief basins: examples from the Slave Province, Northwest Territories, Canada. In: Altermann, W., Corcoran, P.L. (Eds.), *Precambrian Sedimentary Environments: A modern Approach to Ancient Depositional Systems: Special Publication Number 33 of the International Association of Sedimentologists*, p. 183–211.
- Danielson, A., Möller, P., Dulski, P., 1992. The europium anomalies in banded iron formations and the thermal history of the oceanic crust. *Chem. Geol.* 97, 1–12.
- Davis, W.J., Bleeker, W., 1999. Timing of plutonism, deformation, and metamorphism in the Yellowknife Domain, Slave Province, Canada. *Canad. J. Earth Sci.* 36, 1169–1187.
- Davis, W.J., Fryers, B.J., King, J.E., 1994. Geochemistry and evolution of late Archean plutonism and its significance to the tectonic development of the Slave craton. *Precamb. Res.* 67, 207–241.
- Davis, W., Jones, A., Bleeker, W., Grütter, H., 2003. Lithosphere development in the Slave craton: a linked crustal and mantle perspective. *Lithos* 71, 575–589.
- De Baar, H.J.W., Bacon, M.P., Brewer, P.G., Bruland, K.W., 1985. Rare earth elements in the Pacific and Atlantic Oceans. *Geochim. Cosmochim. Acta* 49, 1943–1959.
- Derry, L.A., Kurtz, A.C., Ziegler, K., Chadwick, O.A., 2005. Biological control of terrestrial silica cycling and export fluxes to water-sheds. *Nature* 433, 728–731.
- Drever, J.I., 1974. Geochemical model for the origin of Precambrian Banded Iron Formations. *Geol. Soc. Am. Bull.* 85, 1099–1106.
- Dymek, R.F., Klein, C., 1988. Chemistry, petrology and origin of banded iron-formation lithologies from the 3800 Ma Isua supracrustal belt, west Greenland. *Precamb. Res.* 39, 247–302.
- Eggleton, R., Chappell, B., 1978. The crystal structure of stilpnomelane Part III Chemistry and physical properties. *Mineral. Mag.* 4, 361–368.
- Ferguson, M., Waldron, W.F., Bleeker, W., 2005. The Archean deep-marine environment: turbidite architecture of the Burwash Formation, Slave Province, Northwest Territories. *Can. J. Earth Sci.* 42, 935–954.
- Frei, R., Polat, A., 2007. Source heterogeneity for the major components of ~3.7 Ga Banded Iron Formations (Isua Greenstone Belt, Western Greenland): tracing the nature of interacting water masses in BIF formation. *Earth Planet. Sci. Lett.* 253, 266–281.
- Frith, R. A., 1987. Precambrian geology of the Hackett River area, District of Mackenzie, NWT. Geological Survey of Canada, Memoir 417, 61 p.
- Froelich, P.N., Blanc, V., Mortlock, R.A., Chillrud, S.N., Dunstan, W., Udomkit, A., Peng, T.-H., 1992. River fluxes of dissolved silica to the ocean were higher during glacial: Ge/Si in diatoms, rivers, and oceans. *Paleoceanography* 7, 739–767.

- Gole, M.J., 1980a. Mineralogy and petrology of very low metamorphic grade Archean banded iron-formations, Weld Range, Western Australia. *Am. Mineral.* 66, 8–25.
- Gole, M.J., 1980b. Low temperature retrograde minerals in metamorphosed Archean banded iron formations, western Australia. *Can. Mineral.* 18, 205–214.
- Gromet, L.P., Haskin, L.A., Korotev, R.L., Dymek, R.F., 1984. The "North American shale composite": Its compilation, major and trace element characteristics. *Geochim. Cosmochim. Acta* 48, 2469–2482.
- Hamade, T., Konhauser, K.O., Raiswell, R., Goldsmith, S., Morris, R.C., 2003. Using Ge/Si ratios to decouple iron and silica fluxes in Precambrian banded iron formations. *Geology* 31, 35–38.
- Haugaard, R., Frei, R., Stendal, H., Konhauser, K., 2013. Petrology and geochemistry of the ~2.9 Ga Itilliarsuk banded iron formation and associated supracrustal rocks, West Greenland: source characteristics and depositional environment. *Precamb. Res.* 229, 150–176.
- Haugaard, R., Pecoits, E., Lalonde, S., Rouxel, O., Konhauser, K., 2016a. The Joffre Banded Iron Formation, Hamersley Group, Western Australia: Assessing the Palaeoenvironment through detailed Petrology and Chemostratigraphy. *Precamb. Res.* 273, 12–37.
- Haugaard, R., Ootes, L., Creaser, R.A., Konhauser, K., 2016b. The nature of Mesoarchean seawater and continental weathering in 2.85 Ga BIF, Slave craton, NW Canada. *Geochimica et Cosmochimica Acta* 194, 34–56.
- Haugaard, R., Ootes, L., Heaman, L.M., Hamilton, M.A., Shaulis, B., Konhauser, K., 2017. Depositional timing of Neoproterozoic turbidites of the Slave craton – recommended nomenclature and type localities. *Can. J. Earth Sci.* 54, 15–32.
- Helmstaedt, H., 2009. Crust–mantle coupling revisited: The Archean Slave craton, NWT, Canada. In: Foley, S., Aulbach, S., Brey, G., Grutter, H., Hofer, H., Jacob, D., Lorenz, V., Stachel, T., Woodland, A. (eds.) Proceedings of the 9th International Kimberlite Conference. *Lithos*, 112: 1055–1068.
- Henderson, J.B., 1970. Stratigraphy of the Archean Yellowknife Supergroup, Yellowknife Bay-Prosperous Lake Area, District of Mackenzie. *Geol. Surv. Can. Pap.* 70–26.
- Henderson, J.B., 1975. Stratigraphy of the Archean Yellowknife Supergroup at Yellowknife, District of Mackenzie. *Geol. Surv. Can. Bull.* 246, 62.
- Holland, H.D., 1973. The oceans: A possible source of iron in iron formations. *Econ. Geol.* 68, 1169–1172.
- Jackson, V.A., 2001. Report on the geology of the northern Russell Lake area (850=4). Northwest Territories Geoscience Office, EGS 2001–03, 90 p.
- Jacobsen, S.B., Pimental-Klose, M.R., 1988. A Nd isotope study of the Hamersley and Michipicoten banded iron formations: The source of REE and Fe in Archean oceans. *Earth Planet. Sci. Lett.* 87, 29–44.
- James, H.L., 1954. Sedimentary facies of iron-formation. *Econom. Geol.* 49, 235–291.
- Jenner, G.A., Fryer, B.J., McLennan, S.M., 1981. Geochemistry of the Archean Yellowknife Supergroup. *Geochim. Cosmochim. Acta* 45, 1111–1129.
- Klein, C., 1974. Greenalite, stilpnomelane, minnesotaite, crocidolite and carbonates in a very low grade metamorphic precambrian iron-formation. *Can. Mineral.* 12, 1–24.
- Klein, C., 2005. Some Precambrian banded iron-formations (BIFs) from around the world: their age, geologic setting, mineralogy, metamorphism, geochemistry, and origins. *Am. Mineral.* 90, 1473–1499.
- Klein, C., Beukes, N.J., 1989. Geochemistry and sedimentology of a facies transition from limestone to iron-formation deposition in the Early Proterozoic Transvaal Supergroup, South Africa. *Econ. Geol.* 84, 1733–1774.
- Klein, C., Gole, M., 1981. Mineralogy and petrology of parts of the Marra Mamba Iron Formation, Hamersley Basin, Western Australia. *Am. Mineral.* 66, 1–19.
- Konhauser, K.O., Pecoits, E., Lalonde, S.V., Papineau, D., Nisbet, E.G., Barley, M.B., Arndt, N.T., Zahnle, K., Kamber, B.S., 2009. Oceanic nickel depletion and a methanogen famine before the Great Oxidation Event. *Nature* 458, 750–754.
- Krapež, B., Barley, M., Pickard, A., 2003. Resedimented origins of the precursor sediments to banded iron formation: sedimentological evidence from the Early Palaeoproterozoic Brockman Supersequence of Western Australia. *Sedimentology* 50 (5), 979–1011.
- Locock, A.J., 2014. An Excel spreadsheet to classify chemical analyses of amphiboles following the IMA 2012 recommendations. *Comput. Geosci.* 62, 1–11.
- Lowe, D.R., 1980. Archean sedimentation. *Ann. Rev. Earth Planet. Sci.* 8, 145–167.
- McLennan, S.M., 1984. Petrological characteristics of Archean graywackes. *J. Sediment. Petrol.* 54, 889–898.
- McLennan, S.M., 1989. Rare earth elements in sedimentary rocks: Influence of provenance and sedimentary processes. In: Lipkin, B.R., McKay, G.A. (Eds.), *Geochemistry and Mineralogy of the Rare Earth Elements*, Vol. 21, pp. 169–196.
- McSwiggen, P.L., Morey, G.B., 2008. Overview of the mineralogy of the Biwabik Iron Formation, Mesabi Iron Range, northern Minnesota. *Regul. Toxicol. Pharmacol.* 52, S11–25.
- Meintzer, R.E., 1987. The mineralogy and geochemistry of the granitoid rocks and related pegmatites of the Yellowknife pegmatite field, NWT. Ph.D thesis, Univ. of Manitoba, 2 Vols., 819 pp., unpubl.
- Mortlock, R.A., Froelich, P.N., Feely, R.A., Massoth, G.J., Butterfield, D.A., Lupton, J.E., 1993. Silica and germanium in Pacific Ocean hydrothermal vents and plumes. *Earth Planet. Sci. Lett.* 119, 365–378.
- Nilsen, T.H., 1980. Modern and Ancient Submarine Fans: Discussion of Papers by R. G. Walker and W. R. Normark. *Am. Assoc. Petrol. Geol. Bull.* 64 (7), 1094–1112.
- Ootes, L., Buse, S., Davis, W.J., Couzens, B.C., 2005. U-Pb ages from the northern Wecho River area, southwestern Slave Province, Northwest Territories: constraints on late Archean plutonism and metamorphism. *Geological Survey of Canada Current Research*, 2005–F2, 13 p.
- Ootes, L., Davis, W.J., Bleeker, W., Jackson, V.A., 2009. Two Distinct Ages of Neoproterozoic Turbidites in the Western Slave Craton: further evidence and implications for a possible back-arc model. *J. Geol.* 117, 15–36.
- Ootes, L., Morelli, R., Lentz, D.R., Falck, H., Creaser, R.A., Davis, W.J., 2011. The timing of Yellowknife gold mineralization: A temporal relationship with crustal anatexis? *Econ. Geol.* 106, 713–720.
- Padgham, W., 1992. Mineral deposits in the Archean Slave Structural Province; lithological and tectonic setting. *Precamb. Res.* 58, 1–24.
- Padgham, W., Fyson, W., 1992. The Slave Province: a distinct Archean craton. *Can. J. Earth Sci.* 29, 2072–2086.
- Pearce, J.A., Harris, N., Trindle, A.G., 1984. Trace element discrimination diagrams for the tectonic interpretation of granitic rocks. *J. Petrol.* 69, 956–983.
- Pecoits, E., Smith, M.L., Catling, D.C., Philippot, P., Kappler, A., Konhauser, K.O., 2015. Atmospheric hydrogen peroxide and Eoarchean iron formations. *Geobiology* 13, 1–14.
- Pehrsson, S.J., 2002. The 2.27–2.63 Ga Indin Lake supracrustal belt: an Archean marginal basin–foredeep succession preserved in the western Slave Province, Canada. In: *Precambrian sedimentary environments: a modern approach to ancient depositional systems*. Edited by W. Altermann and P. Corcoran. Special Publication International Association of Sedimentology 33, 123–152.
- Pehrsson, S., Villeneuve, M., 1999. Deposition and imbrication of a 2670–2629 Ma supracrustal sequence in the Indin Lake area, southwestern Slave Province, Canada. *Can. J. Earth Sci.* 36, 1–21.
- Pickard, A., 2002. SHRIMP U-Pb zircon ages of tuffaceous mudrocks in the Brockman Iron Formation of the Hamersley Range, Western Australia. *Aust. J. Earth Sci.* 49, 491–507.
- Pickard, A.L., Barley, M.E., Krapež, B., 2004. Deep-marine depositional setting of banded iron formation: sedimentological evidence from interbedded clastic sedimentary sequence in the rocks in the early Palaeoproterozoic Dales Gorge Member of Western Australia. *Sed. Geol.* 170, 37–62.
- Polat, A., Frei, R., 2005. The origin of early Archean banded iron formations and of continental crust, Isua, southern West Greenland. *Precambrian Res.* 138, 151–175.
- Rasmussen, B., Meier, D., Krapež, B., Muhling, J., 2013. Iron silicate microgranules as precursor sediments to 2.5-billion-year-old banded iron formations. *Geology* 41, 435–438.
- Rasmussen, B., Krapež, B., Muhling, J.R., 2015. Seafloor silicification and hardground development during deposition of 2.5 Ga banded iron formations. *Geology* 43, 235–238.
- Selley, R.C., 1988. *Applied Sedimentology*. Academic Press, p. 446.
- Sholkovitz, E.R., Landing, W.M., Lewis, B.L., 1994. Ocean particle chemistry: the fractionation of rare earth elements between suspended particles and seawater. *Geochimica et Cosmochimica Acta* 58, 1567–1579.
- Simonson, B.M., 1985. Sedimentological constraints on the origins of Precambrian iron-formations. *Geol. Soc. Am. Bull.* 96, 244–252.
- Steinhofel, G., von Blackenburg, F., Horn, I., Konhauser, K.O., Beukes, N., Gutzmer, J., 2010. Deciphering formation processes of banded iron formations from the Transvaal and the Hamersley Sequence by combined Si and Fe isotope analysis using UV femtosecond laser ablation. *Geochimica et Cosmochimica Acta* 74, 2677–2696.
- Sugitani, K., Yamashita, F., Nagaoka, T., Yamamoto, K., Minami, M., Mimura, K., Suzuki, K., 2006. Geochemistry and sedimentary petrology of Archean clastic sedimentary rocks at Mt. Goldsworthy, Pilbara Craton, Western Australia: evidence for the early evolution of continental crust and hydrothermal alteration. *Precamb. Res.* 147, 124–147.
- Sun, S.-S., McDonough, W.F., 1989. Chemical and isotopic systematics of oceanic basalts: implications for mantle composition and processes. *Geol. Soc. London, Spec. Publ.* 42, 313–345.
- Taylor, S.R., McLennan, S.M., 1985a. *The Continental Crust: Its Composition and Evolution*. Blackwell Scientific, Oxford, p. 312.
- Taylor, S.R., McLennan, S.M., 1985b. *The continental crust: Its composition and evolution*. Blackwell Scientific, Oxford, 312 pages.
- Taylor, S.R., McLennan, S.M., 2009. *Planetary Crusts: Their Composition*. Cambridge University Press, New York, Origin and Evolution, p. 378.
- Tosca, N.J., Guggenheim, S., Pufahl, P., 2016. An authigenic origin for Precambrian greenalite: implications for iron formation and the chemistry of ancient seawater. *Geol. Soc. Am. Bull.* 128, 511–530.
- Trendall, A.F., Blockley, J.G., 2004. Precambrian iron-formation. In: Eriksson, P.G., Altermann, W., Nelson, D.R., Mueller, W.U., Catuneanu, O. (Eds.), *The Precambrian Earth: Tempos and Events*. Developments in Precambrian Geology, 12. Elsevier, Amsterdam, pp. 403–421.
- Van Breemen, O., Davis, W.J., King, J.E., 1992. Temporal distribution of granitoid plutonic rocks in the Archean Slave Province, northwest Canadian Shield. *Canad. J. Earth Sci.* 29, 2186–2199.
- Waychison, W., 2011. Report of Prospecting Activities Conducted in Damoti Lake Area. Merc International Minerals Inc, p. 73.
- Yamashita, K., Creaser, R.A., 1999. Geochemical and Nd isotopic constraints for the origin of late Archean turbidites from the Yellowknife area, Northwest Territories, Canada. *Geochimica et Cosmochimica Acta* 63, 2579–2598.
- Yamashita, K., Creaser, R.A., Stemler, J.U., Zimaro, T.W., 1999. Geochemical and Nd-Pb isotopic systematics of late Archean granitoids, southwestern Slave Province, Canada: constraints for granitoid origin and crustal isotopic structure. *Canadian Journal of Earth Science* 36, 1131–1147.
- Zane, R.J., Lowe, D.R., Morris, W.R., 2012. Climbing-ripple successions in turbidite systems: depositional environments, sedimentation rates and accumulation times. *Sedimentology* 59, 867–898.